

# Accounting for natural uncertainty within monitoring systems for induced seismicity based on earthquake magnitudes

Corinna Roy<sup>1\*</sup>, Andy Nowacki<sup>1</sup>, Xin Zhang<sup>2</sup>, Andrew Curtis<sup>2, 3</sup>, Brian Baptie<sup>4</sup>

<sup>1</sup>University of Leeds, United Kingdom, <sup>2</sup>University of Edinburgh, United Kingdom, <sup>3</sup>ETH Zürich, Switzerland, <sup>4</sup>British Geological Survey, The Lyell Centre, United Kingdom

*Submitted to Journal:*  
Frontiers in Earth Science

*Specialty Section:*  
Solid Earth Geophysics

*Article type:*  
Original Research Article

*Manuscript ID:*  
634688

*Received on:*  
28 Nov 2020

*Revised on:*  
23 Feb 2021

*Journal website link:*  
[www.frontiersin.org](http://www.frontiersin.org)

### *Conflict of interest statement*

The authors declare that the research was conducted in the absence of any commercial or financial relationships that could be construed as a potential conflict of interest

### *Author contribution statement*

CR processed the data, performed the analysis, prepared the figures and wrote the paper. XZ developed the inversion code. BB provided the data of both case studies. All authors contributed to the interpretation of the results and the writing of the paper.

### *Keywords*

Induced seismicity, Local magnitude ML, Uncertainties, Traffic Light System (TLS), hydraulic fracture (HF), Mining, Monte - Carlo method

### *Abstract*

Word count: 141

To reduce the probability of future large earthquakes, traffic light systems (TLS) define appropriate reactions to induced seismicity depending on its local earthquake magnitude ( $M_L$ ). The impact of velocity uncertainties and station site effects may be greater than a whole magnitude unit ( $M_L$ ): this may make the difference between a decision to continue ('green' TLS zone) and an immediate stop of operations ('red' zone). We show how to include these uncertainties in TLS thresholds such that the risk of exceeding a threshold is minimized, or that the certainty of exceedance is maximized. We demonstrate that with the new TLS, a red-light threshold would have been encountered earlier in the hydraulic fracturing operation at Preston New Road, UK, potentially avoiding the later large magnitude events. It is critical to establish systems which permit regulators to account for uncertainties when managing risk.

### *Contribution to the field*

The increase in induced seismicity globally imposes risks to human safety and economic hazard on society, and it increases the importance of understanding and de-risking induced earthquakes. Risk systems, like traffic light systems (TLS) based on the local earthquake magnitude are often used to control our reaction to induced seismicity. Assessing accurate magnitudes for human-induced earthquakes such as those associated with shale gas stimulation, waste water storage, or enhanced geothermal systems is difficult. They are affected by lack of knowledge about the Earth's subsurface between the source and receivers and by the magnitude scale used. Here we propose demonstrate a way to robustly calculate local magnitudes with uncertainties for microseismic events, and to include the uncertainties in the design of traffic light systems (TLS), used for decision-making for induced seismicity. Using recordings of induced seismicity from both shale-gas and mining operations, we show that uncertainties in local earthquake magnitudes are in fact a magnitude unit higher than is currently admitted in risk reduction strategies. We introduce a new method which permits regulators to manage risk despite these higher uncertainties, and show that the method would have tangibly changed decisions concerning the UK events in 2018 at Preston New Road, Lancashire.

### *Funding statement*

This work was supported by the Natural Environment Research Council [grant number NE/R001154/1].

### *Ethics statements*

#### *Studies involving animal subjects*

Generated Statement: No animal studies are presented in this manuscript.

#### *Studies involving human subjects*

Generated Statement: No human studies are presented in this manuscript.

#### *Inclusion of identifiable human data*

Generated Statement: No potentially identifiable human images or data is presented in this study.

*Data availability statement*

Generated Statement: The datasets presented in this study can be found in online repositories. The names of the repository/repositories and accession number(s) can be found below: [https://earthquakes.bgs.ac.uk/data/data\\_archive.html](https://earthquakes.bgs.ac.uk/data/data_archive.html).

In review

# Accounting for natural uncertainty within monitoring systems for induced seismicity based on earthquake magnitudes

Corinna Roy<sup>1,\*</sup>, Andy Nowacki<sup>1</sup>, Xin Zhang<sup>2</sup>, Andrew Curtis<sup>2,3</sup> and Brian Baptie<sup>4</sup>

<sup>1</sup> School of Earth and Environment, University of Leeds, UK

<sup>2</sup> School of GeoSciences, University of Edinburgh, UK

<sup>3</sup> Department of Earth Sciences, ETH Zurich, Switzerland

<sup>4</sup> British Geological Survey, Edinburgh, UK

Correspondence\*:

Corinna Roy

earcroy@leeds.ac.uk

## 2 ABSTRACT

To reduce the probability of future large earthquakes, traffic light systems (TLSs) define appropriate reactions to observed induced seismicity depending on each event's range of local earthquake magnitude ( $M_L$ ). The impact of velocity uncertainties and station site effects may be greater than a whole magnitude unit of  $M_L$ , which can make the difference between a decision to continue ("green" TLS zone) and an immediate stop of operations ("red" zone). We show how to include these uncertainties in thresholds such that events only exceed a threshold with a fixed probability. This probability can be set by regulators to reflect their tolerance to risk. We demonstrate that with the new TLS, a red-light threshold would have been encountered earlier in the hydraulic fracturing operation at Preston New Road, UK, halting operations and potentially avoiding the later large magnitude events. It is therefore critical to establish systems which permit regulators to account for uncertainties when managing risk.

14

15 **Keywords:** induced seismicity, local magnitudes, uncertainties, traffic light system, hydraulic fracturing, mining

## 1 INTRODUCTION

The increasing number of industrial operations related to hydrocarbon extraction, geothermal power production, hydraulic fracturing for shale gas exploitation, wastewater injection, water impoundment, hydrocarbon storage, and mining operations in recent years, and the potential for large-scale subsurface CO<sub>2</sub> storage in future, has increased the importance of understanding and de-risking induced seismicity both to the scientific community and to the public who live near such operations (Grigoli et al., 2017). The potential to induce seismicity by human activities is well known (McGarr et al., 2002; Elsworth et al., 2016; Keranen and Weingarten, 2018; Foulger et al., 2018; Schultz et al., 2020). Military waste fluid injected in the Rocky Mountain Arsenal in the 1960's near Denver, Colorado (Healy et al., 1968), induced the so-called "Denver earthquakes". Since then induced earthquakes related to mining (Arabasz et al., 2005; Fritsch, 2010), oil and gas field depletion, (Bardainne et al., 2008; Van Thienen-Visser and Breunese,

26 shale gas exploitation (Bao and Eaton, 2016; Lei et al., 2019; Clarke et al., 2019), geothermal  
27 exploitation (Häring et al., 2008; Deichmann and Giardini, 2009) and waste water disposal (Ellsworth,  
28 2013) have been documented around the world (Baisch et al., 2019). In the UK, induced earthquakes  
29 related to hydraulic fracturing at Preese Hall (Clarke et al., 2014), and Preston New Road (Clarke et al.,  
30 2019) have been observed, and the latter led to an indefinitely imposed UK government moratorium on  
31 fracking.  
32

33 Traffic light systems (TLS Bommer et al. (2006); Majer et al. (2012); Mignan et al. (2017); Baisch et al.  
34 (2019)) are used widely to manage hazard and risk due to induced seismicity in geothermal and hydrocarbon  
35 industries, whereby operations are continued ("green"), amended ("amber") or stopped ("red") based on  
36 the local event magnitude. In the original TLS developed by Bommer et al. (2006), the TLS thresholds are  
37 based on peak ground velocity, but other TLSs have been implemented based on earthquake magnitude  
38 or other ground motion parameters, such as peak ground acceleration (Ader et al., 2020). Depending on  
39 the industrial activities, criteria for a TLS may be very different. Baisch et al. (2019) and He et al. (2020)  
40 summarized some examples of existing TLSs that correspond to different industrial activities. In the UK the  
41 "amber" and "red" thresholds for induced seismicity related to unconventional oil and gas operations are  
42 set to local earthquake magnitudes  $M_L=0$  and  $M_L=0.5$ , respectively, and this has led to multiple halts of  
43 hydraulic fracturing operations during the past few years (Clarke et al., 2019) and finally to an immediate  
44 moratorium of operations in November 2019.

45 The thresholds between zones in TLS are often defined based on limited case studies and on *a priori*  
46 assumptions in a best effort to provide simple schemes (Grigoli et al., 2017; Baisch et al., 2019).  
47 Consequently, they do not necessarily take into account the range of possible scenarios, nor uncertainties  
48 in event magnitudes, and hence some operations will incorrectly continue, increasing the risk of larger  
49 triggered earthquakes, while others will be wrongly halted. To ensure actions taken are robust, it is therefore  
50 necessary to estimate local magnitudes with uncertainties, and to consider them in the choice of  $M_L$   
51 thresholds in TLSs.  
52

53 Assessing accurate magnitudes for human-induced earthquakes such as shale gas stimulation, waste  
54 water storage, or enhanced geothermal systems is difficult, because they are affected by lack of knowledge  
55 about the Earth's subsurface between the source and receivers and by the magnitude scale used (Kendall  
56 et al., 2019). A standard approach to determine  $M_L$  is to first locate the earthquake and then apply an  
57 empirical scaling relation to the source-to-receiver distance (Gutenberg, 2013; Gutenberg and Richter,  
58 1942). Source location-related uncertainties in  $M_L$  can then be evaluated using the location confidence  
59 ellipses. Unfortunately, estimating errors on  $M_L$  due to velocity model uncertainties, energy attenuation  
60 during propagation or site effects such as wavefield focussing is difficult.  
61

62 It is well known that the accuracy of hypocentre locations depends largely on the velocity model accuracy  
63 (Husen and Hardebeck, 2010). Various efforts have been made to estimate velocity model uncertainties,  
64 by including a correction term to traveltimes curve predictions (Myers et al., 2007), making random  
65 perturbations around a given velocity model (Poliannikov et al., 2013) and by locating seismic events in  
66 an ensemble of velocity models obtained by a Bayesian analysis of independent data (Gesret et al., 2011;  
67 Hauser et al., 2011). Recently, Garcia-Aristizabal et al. (2020) analyzed different sources of uncertainty  
68 that can be relevant for the determination of earthquake source locations, and introduced a logic-tree-based  
69 ensemble modelling approach for framing the problem in a decision-making context. Their approach,

70 however, is not fully probabilistic, but limited to a finite set of explored models.  
 71

72 Here we propose a way to calculate local magnitudes with uncertainties for microseismic events, and to  
 73 include the uncertainties in the design of TLS. We use a 3D Monte Carlo non-linear traveltime tomography  
 74 method to jointly invert for hypocenter locations and velocity model. This allows us to obtain posterior  
 75 distributions for local magnitude  $M_L$ , which cover both velocity and source location uncertainties. Results  
 76 clearly show that velocity uncertainties and station site effects are significant and change the zones of  
 77 the TLS to which events are assigned, hence they directly affect safety related decisions. We then apply  
 78 our method to the hydraulic fracturing induced seismicity at Preston New Road, UK and a mining site,  
 79 and demonstrate that a red-light would have been encountered earlier if uncertainties would have been  
 80 accounted for in the TLS thresholds.  
 81

## 2 METHODS AND DATA

82 Usually, local magnitudes  $M_L$  are calculated by first locating the earthquake using standard linearised  
 83 earthquake location methods (e.g. Klein (2002)), which require simple assumptions about the unknown  
 84 underlying subsurface seismic velocity structure, and then applying an empirical scaling relation to the  
 85 source-receiver distance to determine  $M_L$  (Gutenberg, 2013; Gutenberg and Richter, 1942). The solution  
 86 found by such location methods depends on the *a priori* best guess velocity model, and so it is not  
 87 guaranteed to find a location near that of the true earthquake. They also cannot represent uncertainties on  
 88  $M_L$  related to velocity model uncertainties, energy attenuation during propagation, or site effects such as  
 89 wavefield focussing.  
 90

### 91 2.1 Non-linear joint hypocentre-velocity travel-time tomography

92 We use a probabilistic approach to jointly invert for hypocentre locations and 3D subsurface velocity. Our  
 93 approach is based on a reversible jump Markov chain Monte Carlo algorithm (Green, 1995), which is an  
 94 iterative stochastic method to generate samples from a target probability density. In a Bayesian approach  
 95 all information is described in probabilistic terms. The goal is to calculate the posterior probability  
 96 distribution function (pdf) which describes the probability of model  $\mathbf{m}$  being true given observed data  
 97  $\mathbf{d}$  and other relevant, *a priori* information. The posterior pdf is defined using Bayes' theorem (Jaynes,  
 98 2003): this combines prior knowledge about the model (the prior probability  $p(\mathbf{m})$ ) with a likelihood  
 99 function  $p(\mathbf{d}|\mathbf{m})$  that describes the probability of observing the data if the particular given model  $\mathbf{m}$  was  
 100 true. In our approach, the posterior probability is a trans-dimensional function: the number of parameters  
 101 is not fixed, and hence the posterior pdf is defined across a number of spaces with different dimensionalities.  
 102

103 We use the approach and code of Zhang et al. (2020) and use arrival times of  $P$  and  $S$  body waves from  
 104 local earthquakes as data, and include the velocity model, the average arrival time uncertainties, source  
 105 locations and original time as parameters. The 3D subsurface velocity model is defined in terms of a  
 106 Voronoi tessellation of constant velocity cells, where both the position of Voronoi cells and their number  
 107 can change during sampling, guided by the data and prior information. However, due to the parsimony of  
 108 Bayesian inference, complicated models (models with many cells) tend to be rejected in favour of simpler  
 109 models, if they fit the data equally well. The full model vector  $\mathbf{m}$  is given by

$$\mathbf{m} = (\boldsymbol{\sigma}, n, \mathbf{s}, \mathbf{V}_s, \mathbf{V}_p, \mathbf{e}), \quad (1)$$

110 where  $n$  is the number of Voronoi cells,  $\mathbf{s}$  describes their positions, and  $\mathbf{V}_s$  and  $\mathbf{V}_p$  describe the S- and  
 111 P wave velocity within each Voronoi cell. The vector  $\mathbf{e} = (e_x^1, e_y^1, e_z^1, e_t^1, \dots e_x^N, e_y^N, e_z^N, e_t^N)$  contains  
 112 source locations and origin times of  $N$  events, and  $\sigma$  is the arrival time data uncertainty. The travel time  
 113 uncertainties for event  $i$  are defined as (Zhang et al., 2018):

$$\sigma_i = \sigma_0 t_i + \sigma_1, \quad (2)$$

114 where  $\sigma_0$  and  $\sigma_1$  are noise hyperparameters and  $t$  the  $P$  or  $S$  travel time.  
 115

116 We initialise 20 Markov chains with randomly generated starting models drawn from the prior distribution  
 117 so that each chain starts from a different point in model space. To minimise dependence on this initial  
 118 model, chains progress through a large number of samples called the burn-in phase from which all models  
 119 are discarded. To reduce dependence of each sample on the next, after burn-in we only store every 200th  
 120 model to use as samples of the posterior distribution. Each chain sampled 1.88 million models. At each step  
 121 of the Markov chain a new model  $\mathbf{m}'$  is generated by perturbing the current model. In our approach we have  
 122 seven types of possible perturbation: adding, removing or moving a Voronoi cell (i.e. changing  $\mathbf{s}$ ), changing  
 123 the  $P$  or  $S$  velocity of a randomly chosen Voronoi cell ( $\mathbf{V}_p$ ,  $\mathbf{V}_s$ ), changing the noise hyperparameter  $\sigma$ , or  
 124 changing the source coordinates of one randomly chosen source ( $\mathbf{e}$ ). The type of perturbation is selected  
 125 randomly at each iteration, and the candidate model  $\mathbf{m}'$  is accepted with a probability  $\alpha$  (Green, 1995)  
 126 given by:

$$\alpha(\mathbf{m}'|\mathbf{m}) = \min \left[ 1, \frac{p(\mathbf{m}')}{p(\mathbf{m})} \frac{q(\mathbf{m}|\mathbf{m}')}{q(\mathbf{m}'|\mathbf{m})} \frac{p(\mathbf{d}_{obs}|\mathbf{m}')}{p(\mathbf{d}_{obs}|\mathbf{m})} |\mathbf{J}| \right] \quad (3)$$

127 where  $\mathbf{J}$  is the Jacobian matrix of the transformation from  $\mathbf{m}$  to  $\mathbf{m}'$  and is used to account for the volume  
 128 changes of parameter space during jumps between dimensions, and  $q(\mathbf{m}|\mathbf{m}')$  are proposal distributions that  
 129 we use to propose new models  $\mathbf{m}'$  at each step. In our case, it can be shown that the Jacobian is an identity  
 130 matrix (Zhang et al., 2018).

131 A key function in the acceptance probability is the likelihood  $p(\mathbf{d}|\mathbf{m})$  which quantifies the misfit between  
 132 the observed data  $\mathbf{d}_{obs}$  and estimated data  $\mathbf{d}_{est}$  obtained by an eikonal solver using the fast marching  
 133 method (Rawlinson and Sambridge, 2004) in model  $\mathbf{m}$ . The likelihood is defined as:

$$p(\mathbf{d}|\mathbf{m}) \propto \exp \left( \frac{-\phi(\mathbf{m})}{2} \right) \quad (4)$$

134 where

$$\phi(\mathbf{m}) = \sum_i \frac{(d_{obs}^i - d_{est}^i)^2}{\sigma_i^2} \quad (5)$$

135 and  $\sigma_i$  is the  $P$  or  $S$  wave travel time uncertainty for event  $i$  given by equation 2. The likelihood function  
 136 contains both the effect of the errors in the source locations and the velocity model uncertainties on the  
 137 travel times. We choose uniform priors for the source location coordinates and the number of Voronoi cells,  
 138 and Gaussian priors for all other parameters. A full and more detailed description of the methodology can  
 139 be found in Zhang et al. (2020, 2018).

140 **2.2  $M_L$  Scaling relations**

141 A general local magnitude scaling relation is described by

$$M_L = \log_{10}(A) + a \log_{10}(r) + br + c + d \exp(f r), \quad (6)$$

142 where  $r$  is the hypocentral distance in km, and  $A$  is the zero-to-peak amplitude in nm on the horizontal  
 143 components filtered with a Wood-Anderson response (Ottemöller and Sargeant, 2013; Butcher et al., 2017;  
 144 Luckett et al., 2018). Parameters  $a$ ,  $b$ ,  $c$ ,  $d$  and  $f$  are region dependent constants which describe the  
 145 geometrical spreading ( $a$ ), attenuation ( $b$ ), the base level ( $c$ ), and distance dependent correction terms ( $d$   
 146 and  $f$ ), respectively.

147 The original BGS scaling relation given by (Ottemöller and Sargeant, 2013) is

$$M_L^{OS} = \log_{10}(A) + 1.11 \log_{10}(r) + 0.00189r - 2.09. \quad (7)$$

148 This was updated by Butcher et al. (2017) to account for short source-receiver distances, giving

$$M_L^B = \log_{10}(A) + 1.17 \log_{10}(r) + 0.0514r - 3. \quad (8)$$

149 The  $M_L$  scaling relation now used by the BGS (Luckett et al., 2018) is:

$$M_L^L = \log_{10}(A) + 1.11 \log_{10}(r) + 0.00189r - 1.16 \exp(-0.2r) - 2.09. \quad (9)$$

150 The latter scale was used for the BGS locations throughout this paper.

151 **2.3 Data**

152 We use data from surface seismic monitoring arrays at two sites in the United Kingdom: (1) Preston New  
 153 Road, where hydraulic fracturing took place in the Bowland Shale tight gas reservoir, and (2) Thoresby  
 154 Colliery, a deep coal mine in Nottinghamshire.

155

156 At Preston New Road, hydraulic fracturing started on 15 October 2018 at the PNR-1z well in Lancashire,  
 157 UK under the guidance of Cuadrilla Resources Ltd. and targeted the Bowland shale at a depth of  $\sim$ 2300 m  
 158 (Clarke et al., 2019). During operations, the British Geological Survey (BGS) detected 172 local seismic  
 159 events with local magnitudes  $M_L$  between  $-1.8$  and  $1.6$ . The  $M_L=0$  threshold (“amber”) was exceeded  
 160 by nine events, six of which had local magnitudes larger than  $0.5$  (“red” zone). In late October 2018, five  
 161 events occurred that exceeded the red light TLS thresholds after which operations were paused for a month,  
 162 but microseismicity still occurred during the hiatus (Figure 1). The largest event with  $M_L=1.6$ , which  
 163 was felt by some local residents, occurred on 11 December 11:21:15 UTC after operations resumed on 8  
 164 December. Hydraulic fracturing operations of the well ended on 17 December 2018. Over the course of  
 165 three months more than 38,000 microseismic events were detected in real-time with the geophone array,  
 166 with moment magnitudes  $M_w$  between  $-3.1$  to  $1.6$  (Clarke et al., 2019). We analysed the  $P$ - and  $S$ -wave  
 167 travel time data for the 172 largest earthquakes which were recorded at 11 seismic stations by the BGS  
 168 (Figure 2). The majority of these events occurred between 2 and 2.5 km depth and occur in the vicinity of  
 169 the well.

170

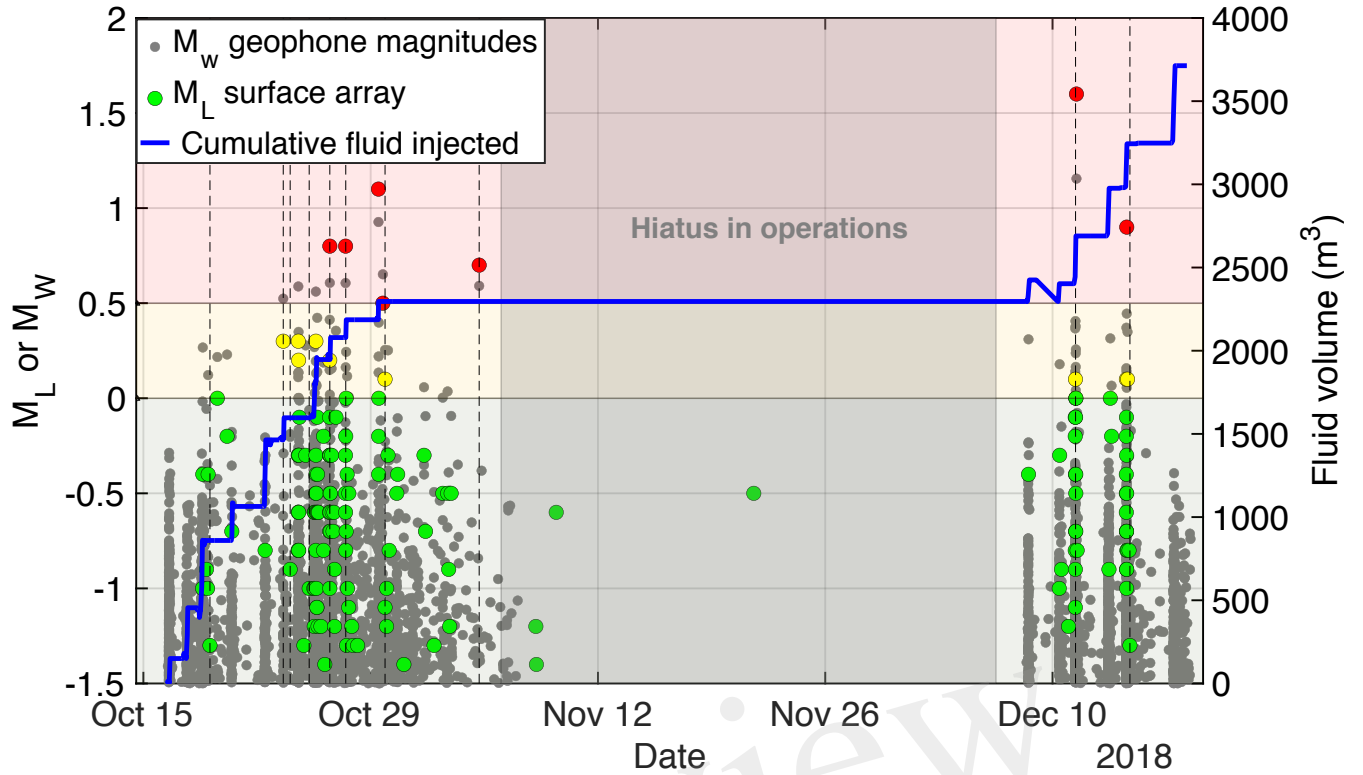


**Figure 1.** Induced seismicity at hydraulic fracturing site at Preston New Road, UK. Background colors indicate the three zones of the UK TLS. Smaller gray dots show the moment magnitude ( $M_w$ ) for events observed on the dowhole geophone array. Larger dots show the local magnitude ( $M_L$ ) for events observed by the surface seismometer array, and are color-coded by the TLS zone into which they fall. The blue line shows the cumulative volume of fluid injected into the well.

### 171 2.3.1 Thoresby Colliery

172 Thoresby Colliery in New Ollerton has a history of seismicity related to mining (Bishop et al., 1993),  
 173 and in response to felt earthquakes between December 2013 and January 2014, the British Geological  
 174 Survey (BGS) installed a temporary seismic network with seven seismometer stations, four of which are  
 175 three-component broadband stations (Figure 3). Mining-induced earthquakes are some of the most widely  
 176 studied and their magnitude and depth range is similar to fracking induced earthquake magnitudes (Davies  
 177 et al., 2013), hence provide an excellent analog for the study of hydrofracturing induced seismicity.

178 Most of the seismic events used in this study are located north and south of the coal seams (Figure 3),  
 179 and the majority of the events occurs at 800 m depth, which coincides with the depth of the coal seams  
 180 (Butcher et al., 2017). The northern cluster occurred later in 2014 than the southern one. To reduce the  
 181 computational costs we only use 61 seismic events out of the 305 recorded, giving 769  $P$ - and  $S$  travel  
 182 times to invert.

## 3 RESULTS

183 The McMC joint inversion provides us 3D posterior distributions of seismic velocities ( $V_p$  and  $V_s$ ), and  
 184 of the earthquake hypocenter locations (Figure 4a,b). Therefore, we can calculate hypocentral distance  
 185 posterior distributions (Figure 4c), which in turn allows us to estimate station-average local magnitudes  $M_L$   
 186 posterior distributions (4d) using a scaling relation (e.g one of equations 6-8). These distributions include  
 187 the effects of velocity and source location uncertainties as well as the source radiation pattern on the pdf

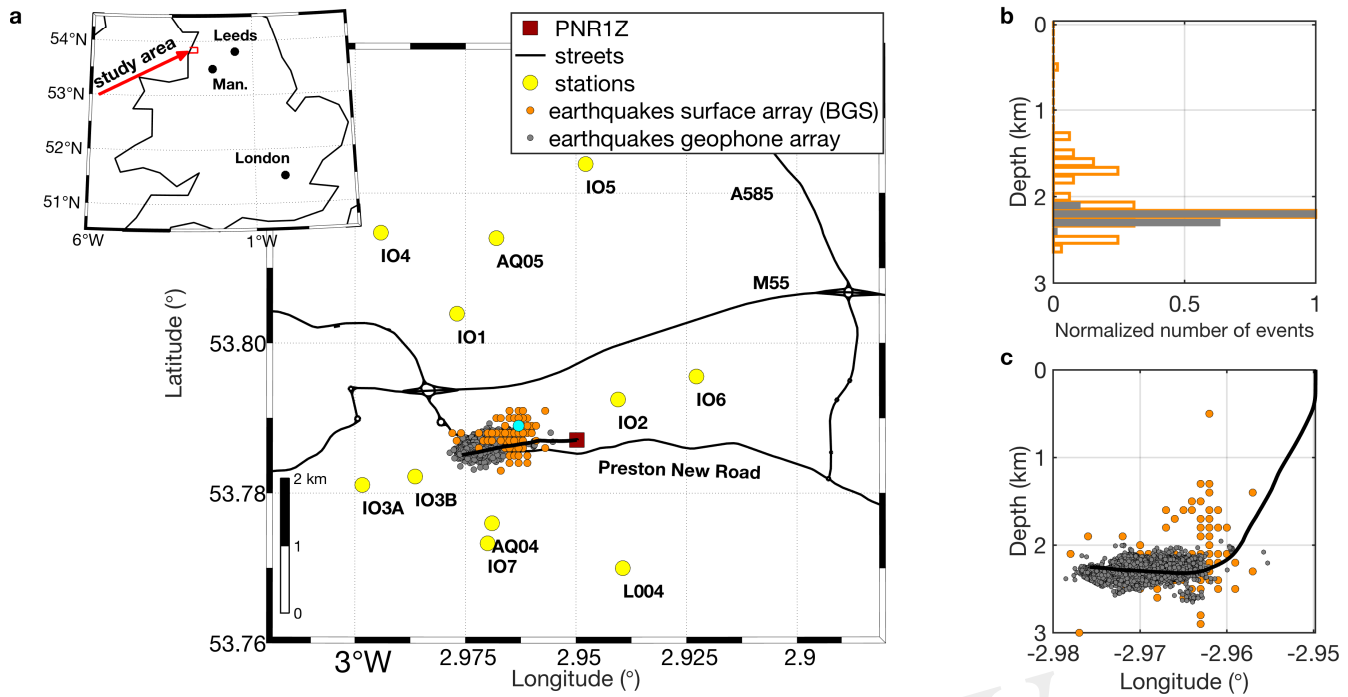


**Figure 2.** Seismicity at Preston New Road. **(a)** Seismic stations (yellow dots) near the Preston New Road hydraulic fracturing site near Blackpool (location shown in inset) and seismic events used in this study (orange dots). The injection well is shown by a black line. The cyan dot marks an earthquake discussed in Figure 5. **(b)** Histogram of depth distribution of the seismic events recorded at the surface array (orange) and the downhole geophone array (grey). **(c)** Distribution of seismic events.

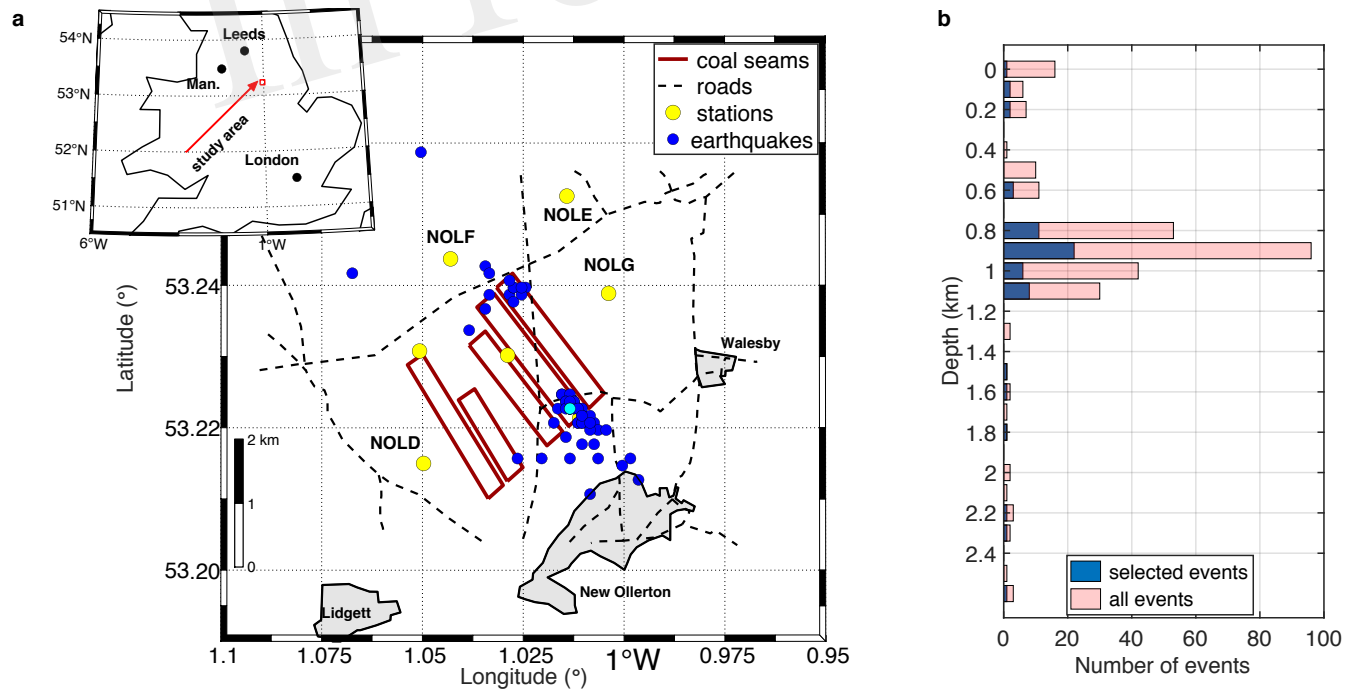


**Figure 3.** Seismicity at the Thoresby Colliery mining site. **(a)** Seismic stations (yellow dots) near the UK's last deep coal mine in New Ollerton (location shown in inset) and seismic events used in this study (blue dots). The coal seam mine galleries are outlined by red rectangles. **(b)** Depth distribution of the seismic events as determined by the British Geological Survey. Depths for all events in the catalog are shown in pink; the blue bars correspond to the subset of the catalog used in this study.

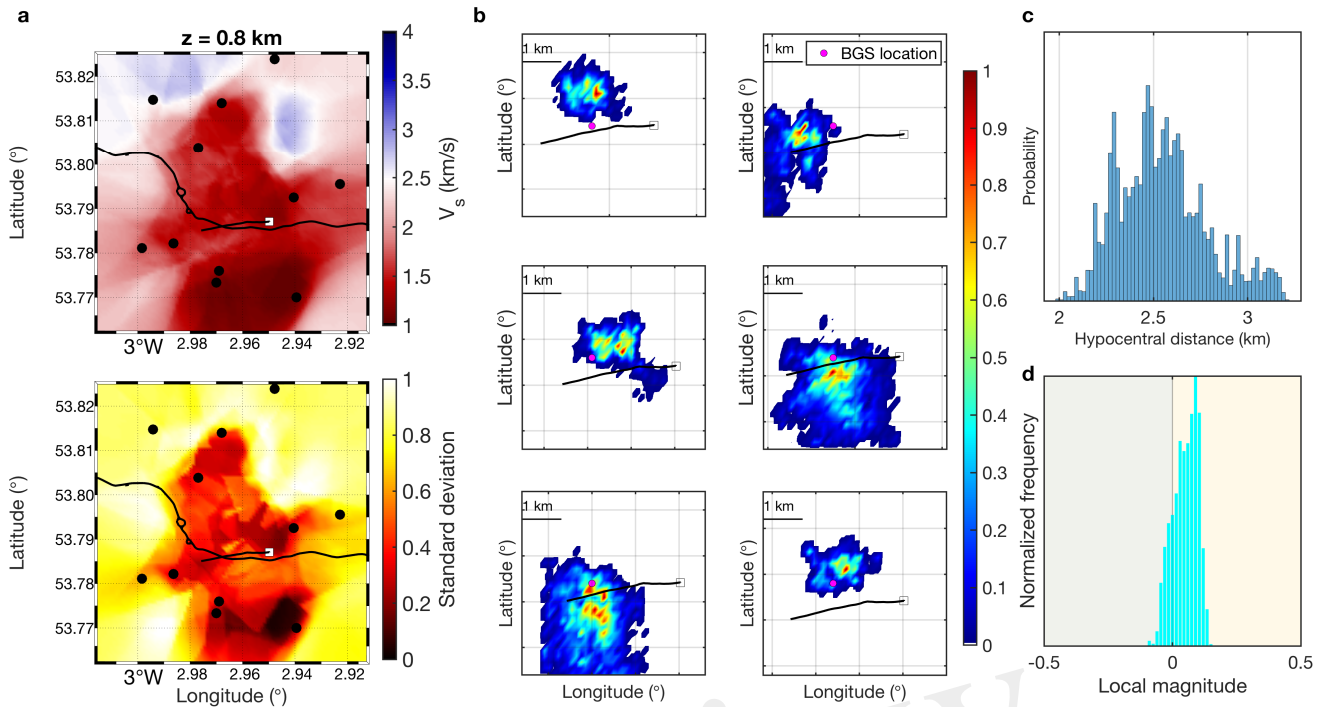


**Figure 4.** Results of the McMC joint hypocentre-velocity tomography at Preston New Road. **(a)** Shear wave velocity  $V_s$  at 0.8 km depth and its standard deviation. **(b)** Posterior probability distribution of hypocentre locations in longitude-latitude for six different sources. **(c)** Posterior probability distribution of hypocentral distance of one source to one station. **(d)** Posterior probability distribution of local magnitude of the same event as in (c), calculated from the hypocentral distance using the scaling relation in equation (8).

188 for event magnitudes. The station-averaged  $M_L$  posterior distribution for one source may have a width that  
 189 spans more than one zone of the traffic light system (e.g. cyan distribution in Figure 4d) which indicates  
 190 that velocity model uncertainties alone can change the TLS zone to which the earthquake is attributed.  
 191 Thus, uncertainties affect real operational decisions.  
 192

### 193 3.1 Scaling relation and station site effects on $M_L$

194 Figure 5 summarizes uncertainties in  $M_L$  due to scaling relation and station site effects at one station at  
 195 Preston New Road. We observe that the particular choice of  $M_L$  scaling relation affects the local magnitude  
 196 and is itself large enough to change the TLS zone. Local magnitudes are more than half a magnitude unit  
 197 larger using the original BGS scaling relation ( $M_L^{OS}$ , equation (6)) compared to the most recent scale ( $M_L^L$ ,  
 198 equation (8)) (Figure 5a; Supplementary Figure S1) and therefore make a difference between a continuation  
 199 ("green") and an immediate stop ("red"). Note, however, that the original BGS scaling relation was not  
 200 used by the BGS to calculate  $M_L$  for these events; we include it here to show the effect of magnitude  
 201 scale choices. The difference in  $M_L$  between the  $M_L^B$  scale (equation (7)) and the most recent UK scaling  
 202 relation  $M_L^L$  (equation (8)) are smaller, but peaks of distributions can lie in different zones of the TLS  
 203 (Figure 5a).  
 204

205 Station site effects such as attenuation, focussing and radiation pattern become evident by comparing  
 206  $M_L$  distributions at individual stations. These uncertainties can shift the  $M_L$  posterior distribution for one

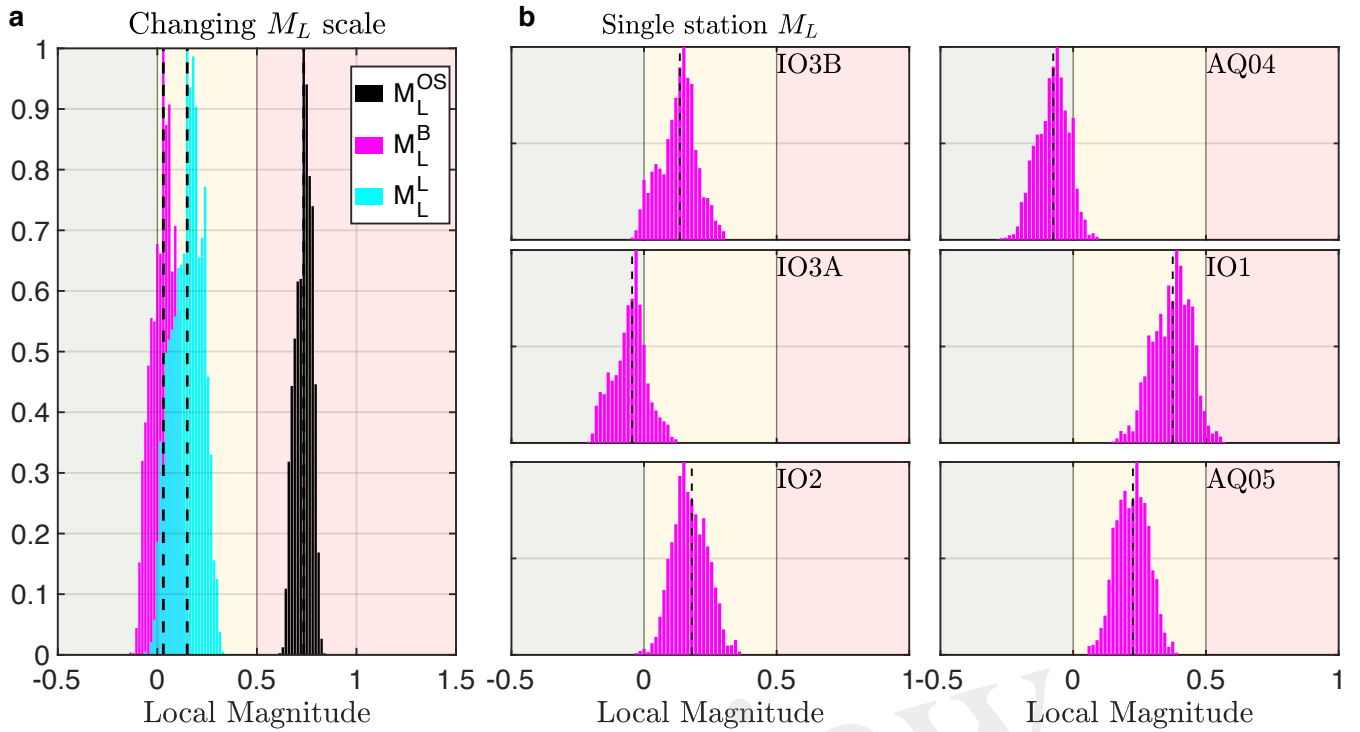


**Figure 5.** Effect of scaling relation and station site effects on  $M_L$  for Preston New Road stations. Local earthquake magnitude  $M_L$  posterior probability distributions for the cyan coloured earthquake in Figure 1. **(a)** Effect of the local magnitude scaling relation Ottemöller and Sargeant (2013); Butcher et al. (2017); Luckett et al. (2018) (equations 6-8). **(b)** Single-station magnitudes at 6 stations using equation (7). Background colours indicate the zones of the UK traffic light system Department of Energy and Climate Change (2013). Dashed lines indicate the mean.

source by half a magnitude unit, sometimes more, easily sufficient to move the source into another zone of the TLS (Figure 5b ; Supplementary Figure S2). We compare velocity and station site effect uncertainties on local magnitudes in Figure 6 for the hydraulic fracturing induced earthquakes at Preston New Road. The site effect uncertainties are estimated by calculating the mean local magnitude for each seismic source at all 4 stations (using the amended BGS scaling relation, equation (8)), and then taking the difference between the smallest and largest mean station magnitude as a measure of site-related uncertainties. The velocity-related uncertainties are defined as the width of the interval between the 5-95% percentile of the station-averaged local magnitudes distributions. Their effects each average around  $\pm 0.125$  and  $\pm 0.05$  magnitude units, respectively, in our case study, but they vary and can have a combined effect that alters magnitude estimates by up to a whole magnitude unit (Figure 6). We observe that uncertainties are also roughly equally important for the mining induced seismicity at New Ollerton - their effects average around  $\pm 0.3$  and  $\pm 0.05$  magnitude units for site and velocity-related effects, respectively - with a combined effect that again can alter magnitude estimates by up to a whole magnitude unit, and potentially move events from "green" to "red" zones (Figure 7).

221

#### 4 A PROBABILISTIC TRAFFIC LIGHT SYSTEM

We can now include the velocity and station site effect uncertainties in  $M_L$  in a traffic light system (TLS). To do this, we first calculate  $M_L$  threshold probability curves using the station-averaged  $M_L$  posterior distributions of the microseismic events at Preston New Road. Threshold probability curves describe the

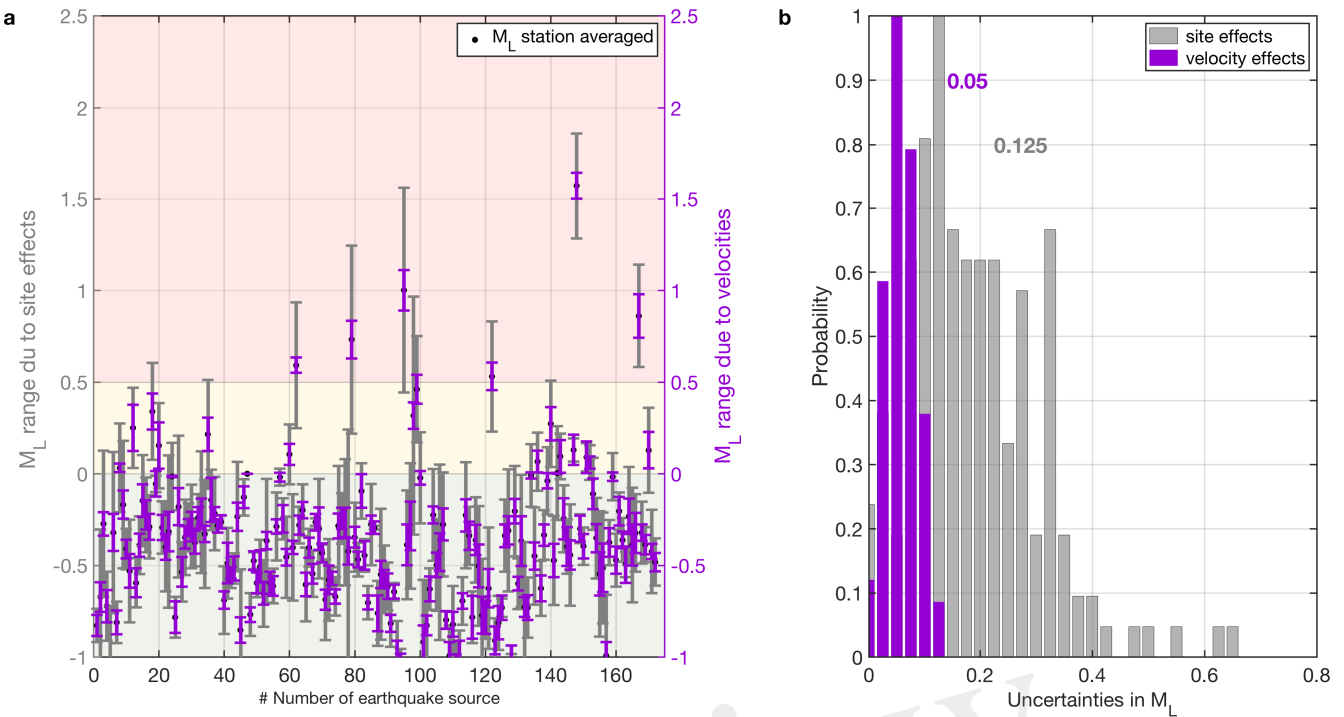


**Figure 6.** Comparison of velocity and station site effect uncertainties on local magnitudes at Preston New Road. (a) Uncertainties on the station-averaged magnitude calculated with the amended BGS scale (equation (8)) due to velocity uncertainties (purple error bars) and station site effects (grey bars). Black dots mark the maximum of the station-averaged  $M_L$  distribution for each seismic event. Background colours indicate the three zones of the UK traffic light system, “green”, “amber” and “red”. (b) Normalised histograms of the magnitude uncertainties displayed in a). Numbers display the velocity and station-site effect uncertainties at which the histograms take maximum values.

225 probability that an earthquake of a given magnitude is in any one zone of the TLS. They take into account  
 226 velocity and station-site effect uncertainties, as well as attenuation and geometrical spreading in  $M_L$ .  
 227 Furthermore, the threshold probability curves allow us to draw conclusions about the range of observed  
 228  $M_L$  for which the probability of any earthquake being in a zone drops below a given confidence level  $\alpha$ .  
 229 The last point is particularly interesting for regulators and operators because it enables them to define the  
 230 thresholds between zones in such a way that the probability of an earthquake being in each zone of the  
 231 TLS is always above a chosen confidence level  $\alpha$ .  
 232

233  $M_L$  threshold probability curves are obtained by shifting each of the 172 station-averaged event  $M_L$  pdfs  
 234 along the local magnitude axis and estimating the percentage of the distribution lying in each of the three  
 235 zones of the TLS (Supplementary Figure S3). By averaging over all threshold probabilities curves, we  
 236 obtain one curve that describes the probability of an earthquake with a given magnitude being in any zone  
 237 of the TLS. This can then be used to draw conclusions about (1) probabilities of earthquakes of a certain  
 238 event magnitude  $M_L$  being in any one of the TLS zones, and (2) the  $M_L$  range for which the probability of  
 239 any earthquake being in a zone drops below a given confidence level  $\alpha$ .  
 240

241 Our approach here is approximate, but once the first inversion if performed, subsequent assignment of a  
 242 new event’s  $M_L$  to the correct zone of an adjusted TLS is trivial and can be done in real time, as explained

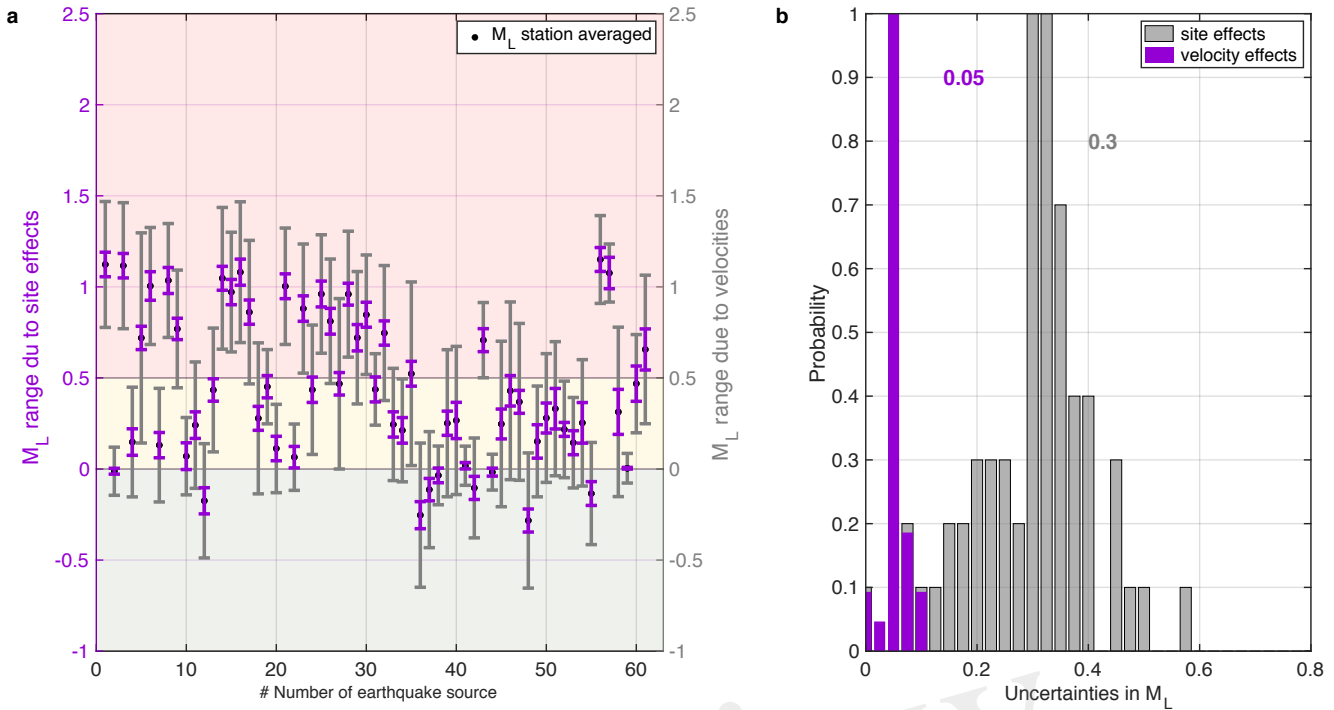


**Figure 7.** Same as Figure 6 for local magnitudes at New Ollerton mining site.

243 below. In theory, however, the most rigorous approach to incorporating uncertainty into the calculation  
 244 of  $M_L$  for any one event is to retrieve its full posterior  $M_L$  distribution, which is the averaged pdf across  
 245 all stations for that one event. Although at this point we can do this for any existing event in our dataset,  
 246 in practice we want to be able to do this for each new event that occurs, in real time. This presents a  
 247 large challenge, however, since formally we must add the travel times from this new event to our dataset  
 248 and re-run the whole sampling procedure again. We have added one new earthquake to the dataset and  
 249 sampled 140,000 new models. This took 14,880 CPU-hours on the ARCHER HPC machine, and so remains  
 250 practically impossible for real time monitoring. Furthermore, the  $M_L$  pdf of the new event is still sparsely  
 251 sampled, and hence does not allow for a robust  $M_L$  uncertainty quantification.

#### 252 4.1 TLS with realistic uncertainties

253 A regulator or operator can choose whether they wish to minimise the probability of any such event  
 254 exceeding a TLS threshold undetected, or to maximise the certainty that an event truly has exceeded the  
 255 legal magnitude limits in order to avoid unnecessary, costly halt of operations. We term the first  $TLS^-$ ,  
 256 where the  $M_L$  thresholds are shifted toward smaller apparent-magnitude thresholds. In this way, the risk of  
 257 smaller-magnitude events leading to large earthquakes is reduced because operations are both halted and  
 258 put "on caution" earlier. In the latter, the TLS thresholds would effectively be increased to higher values  
 259 ( $TLS^+$ ), so that operations could still continue up to larger apparent earthquake magnitudes. The choice of  
 260 the risk system by the operator ( $TLS^+$  or  $TLS^-$ ) is, however, subjective and depends on the country's  
 261 governmental policies. The choice of the confidence level defines the TLS thresholds, but these as well as  
 262 the risk strategy can be changed at any time.  
 263

264 For example, say a regulator or operator chooses that the confidence level with which each event is  
 265 assigned to the correct zone must be at least 80% for decisions to be made. The range of estimated  $M_L$

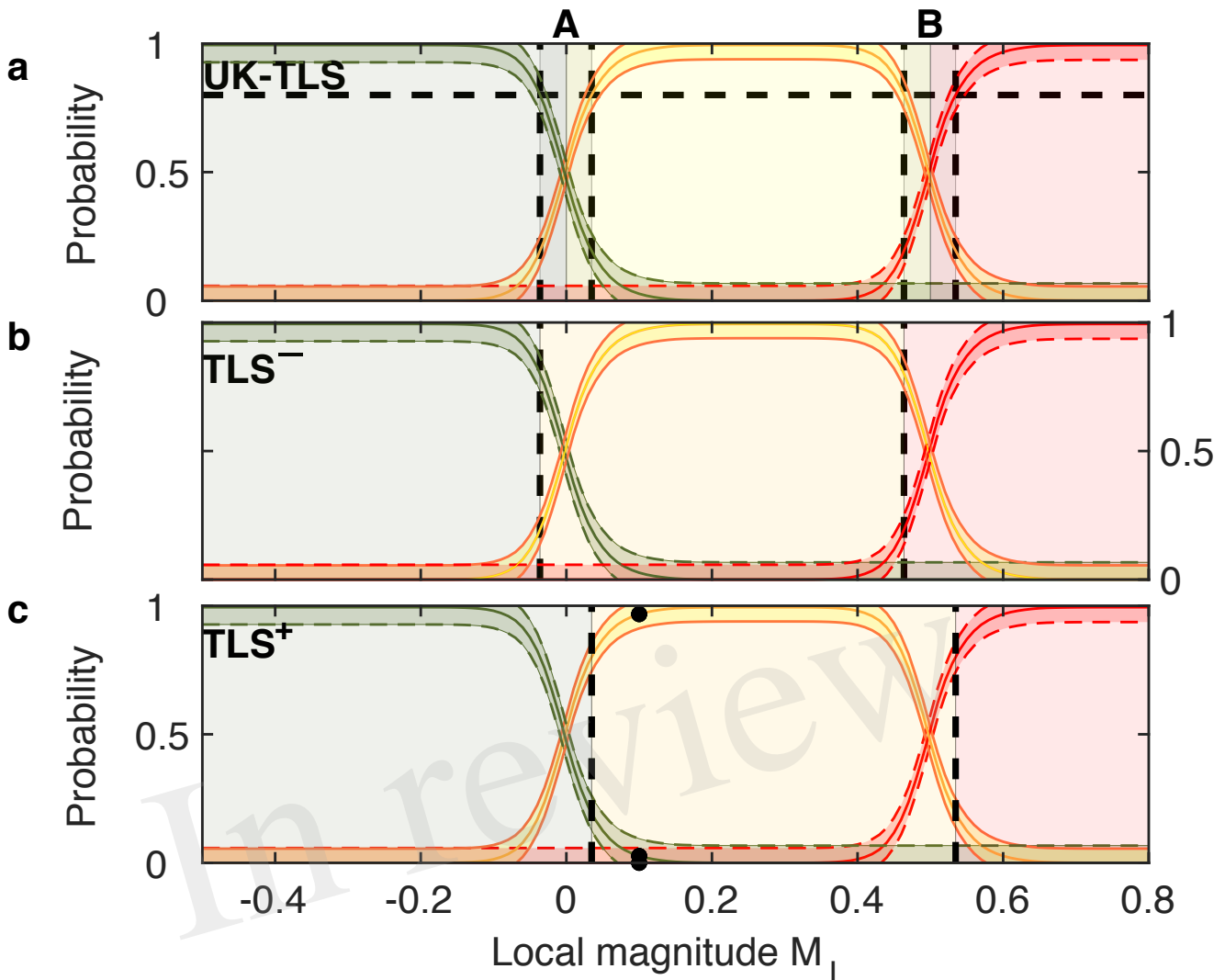


**Figure 8.** Developing TLS systems where the risk of larger triggered earthquakes is potentially reduced ( $TLS^-$ ), and a TLS where the risk of unnecessary, costly stop of operations is reduced ( $TLS^+$ ). The threshold probability curves describe the probability of an event of local magnitude  $M_L$  being in any one of the TLS zones (colour coded red/amber/green for each zone). **(a)** Earthquakes that have  $M_L$  estimates in zones A and B cannot be assigned to “red/amber/green” with 80% confidence. **(b)** For a 20% risk of an event exceeding a TLS threshold undetected, zones A and B are attributed to “amber” and “red”, respectively ( $TLS^-$ ). **(c)** For 80% certainty that any event has exceeded a threshold, zones A and B are attributed to “green” and “amber”, respectively ( $TLS^+$ ). Black dots in c) mark probabilities for example earthquakes of different  $M_L$ .

values that would have less than  $\alpha = 0.8$  probability is  $-0.036 < M_L < 0.035$  (zone A) and  $0.46 < M_L < 0.53$  (zone B) (grey zones in Figure 8a) using the current UK TLS thresholds. Then, in a  $TLS^-$ , all of zone A would be attributed to “amber”, and zone B to “red”, effectively moving the TLS thresholds to lower values (Figure 8b). Alternatively, in a  $TLS^+$ , zone A would be assigned to “green” and zone B to “amber”, so the TLS thresholds would effectively be increased to higher values (Figure 8c).

The uncertainties in  $M_L$  discussed here are site specific so need to be determined for each geographical area or industrial operation individually. However, our approach can be applied to any site and to any form of induced seismicity. We have also demonstrated that for the Thoresby Colliery mining site in the UK

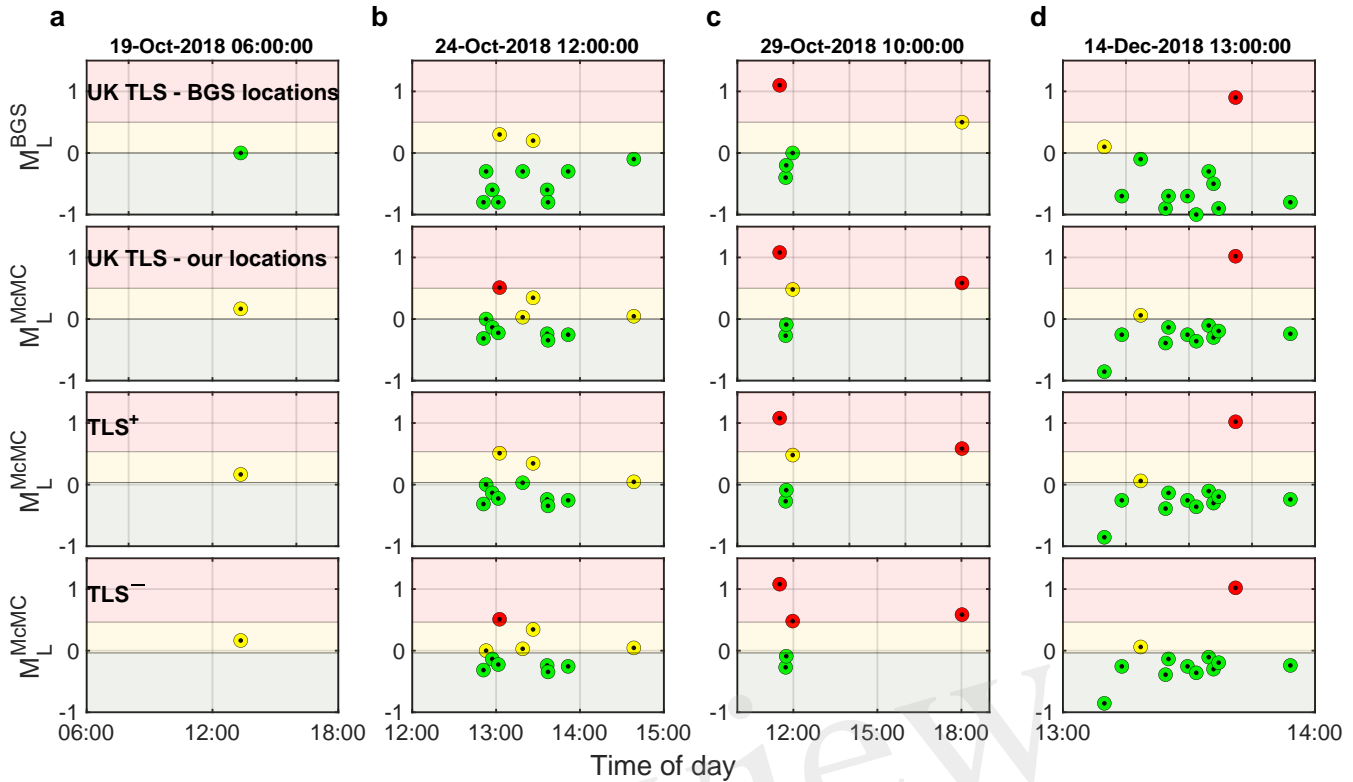


**Figure 9.** Classification of seismic events for four days (columns) in the UK TLS (top two rows). Row 1 shows results using the local magnitudes determined by the BGS while other rows use the maximum probability magnitude determined in this work. Row 3: Classifications for a TLS where the risk of unnecessary, costly stop of operations is reduced ( $TLS^+$ ). Row 4: TLS where the risk of larger triggered earthquakes is potentially reduced ( $TLS^-$ ). Both were calculated for an 80% confidence level.

274 the velocity model and station site effect uncertainties in  $M_L$  are non-negligible (Figure 7), and can be  
 275 accounted for in the choice of TLS thresholds (Supplementary Figure S4).

## 5 APPLICATION OF A PROBABILISTIC TLS TO PRESTON NEW ROAD SEISMICITY

276 We can use the three TLSs (Figure 8) to analyze retrospectively how decisions would have changed at  
 277 Preston New Road under a  $TLS^+$  or  $TLS^-$  (Figure 9). We compare here the classification in the UK-TLS,  
 278 a  $TLS^-$  and  $TLS^+$  for a 80% confidence level. (Figure 5). That means, the risk of exceeding a TLS  
 279 threshold in  $TLS^-$  is 20%, while in the  $TLS^+$ , the certainty that a threshold was exceeded is 80%. The  
 280 earthquake on October 19th would have been classified as “amber” in all three TLSs using the maximum  
 281 probability magnitude, whereas it was classified as “green” by the operator. Hence, action would have been  
 282 taken earlier and the probability of subsequent larger events would have been reduced. The same is true  
 283 for the seismicity on October 24th (Figure 9b), where operations would have stopped immediately with a  
 284 safety prioritising system ( $TLS^-$ ), and also in the UK TLS with a  $M_L$  that accounts for uncertainties. This  
 285 demonstrates the importance of accounting for uncertainties in local magnitudes  $M_L$  in the decision-making  
 286 process.  
 287

We acknowledge that the occurrence of induced seismicity is a multi-parameter phenomenon, depending on details of subsurface structures as well as on the complete history of operational measures and therefore cannot be predicted. Deformation processes may continue and can still induce seismicity after injections stop. The delay time between hydraulic fracturing completion and the cessation of the observed seismicity can be up to several years (Baisch et al., 2019). It is therefore speculative that an earlier stop would have prevented large magnitude post-injection seismicity at PNR. Nevertheless, it has been shown that lower  $M_L$  threshold values in the TLS used for the geothermal stimulation in Basel, Switzerland could have prevented larger magnitude post-injection seismicity (Baisch et al., 2019). We therefore argue that it is critical to establish systems which permit regulators to account for uncertainties while managing risk, as we propose here.

## 6 CONCLUSIONS

We implemented a fully Bayesian approach for analysing uncertainties, such as velocity model and source location uncertainties in local earthquake magnitudes and evaluate their influence on decision-making for induced seismicity. We conclude that these uncertainties are important, as they can make a difference of up to one or two magnitude unit, and hence directly affect operational decisions by potentially moving an earthquake two zones in a traffic light system (TLS) leading to radically different operational outcomes.

To build a site-specific probabilistic TLS that accounts for uncertainties, the following three steps are necessary: 1) run one fully nonlinear hypocentre-velocity tomography for the site and calculate  $M_L$  posterior distributions for each earthquake. 2) calculate threshold probability curves, choose a desired confidence level  $\alpha$ , and determine the  $M_L$  zones A and B below the desired confidence level. 3) attribute zone A and B to “green/amber” or “amber/red” according to the desired safety system (reduce the risk of larger magnitude events ( $TLS^-$ ) or reduce the risk of halting operations unnecessarily ( $TLS^+$ )). From this point on, real time assignment of any new event’s  $M_L$  to the correct TLS zone is trivial, yet incorporates all the uncertainty in the measurements.

312

We applied our method to anthropogenic seismicity at a hydraulic fracturing site in the UK, and demonstrate that a red-light threshold would have been encountered earlier in a  $TLS^-$ , which possibly could have prevented the UK-wide shut-down. We also applied our methods to mining-related seismicity at Thoresby Colliery, UK and find they apply equally well in this different setting. Hence, our approach can be applied to any site and any form of seismicity.

## CONFLICT OF INTEREST STATEMENT

The authors declare that the research was conducted in the absence of any commercial or financial relationships that could be construed as a potential conflict of interest.

## AUTHOR CONTRIBUTIONS

CR processed the data, performed the analysis, prepared the figures and wrote the paper. XZ developed the inversion code. BB provided the data of both case studies. All authors contributed to the interpretation of the results and the writing of the paper.

## FUNDING

This work was supported by the Natural Environment Research Council [grant number NE/R001154/1].

## ACKNOWLEDGMENTS

324 This work used the ARCHER UK National Supercomputing Service (<http://www.archer.ac.uk>) and ARC3,  
325 part of the High Performance Computing facilities at the University of Leeds, UK. The authors thank  
326 the Edinburgh Interferometry Project sponsors for supporting this research. We thank two anonymous  
327 reviewers for their comments to improve this manuscript.

## SUPPLEMENTAL DATA

### DATA AVAILABILITY STATEMENT

328 Data were provided by the BGS and can be downloaded from the webpage ([https://earthquakes.bgs.ac.uk/data/data\\_archive.html](https://earthquakes.bgs.ac.uk/data/data_archive.html)). The posterior probability density  
329 functions for the earthquake locations and velocity structure are available upon request. The code  
330 used to perform the Bayesian joint hypocenter-velocity inversion of travel time data is available at  
331 <https://github.com/xin2zhang/MCTomo>.

## REFERENCES

- 333 Ader, T., Chendorain, M., Free, M., Saarno, T., Heikkinen, P., Malin, P. E., et al. (2020). Design and  
334 implementation of a traffic light system for deep geothermal well stimulation in Finland. *Journal of*  
335 *Seismology* 24, 991–1014. doi:10.1007/s10950-019-09853-y
- 336 Arabasz, W. J., Nava, S. J., McCarter, M. K., Pankow, K. L., Pechmann, J. C., Ake, J., et al. (2005).  
337 Coal-Mining Seismicity and Ground-Shaking Hazard: A Case Study in the Trail Mountain Area, Emery  
338 County, Utah. *Bulletin of the Seismological Society of America* 95, 18–30. doi:10.1785/0120040045
- 339 Baisch, S., Koch, C., and Muntendam-Bos, A. (2019). Traffic Light Systems: To What Extent Can Induced  
340 Seismicity Be Controlled? *Seismological Research Letters* 90, 1145–1154. doi:10.1785/0220180337
- 341 Bao, X. and Eaton, D. W. (2016). Fault activation by hydraulic fracturing in western Canada. *Science* 354,  
342 1406–1409. doi:10.1126/science.aag2583
- 343 Bardainne, T., Dubos-Sallée, N., Sénéchal, G., Gaillot, P., and Perroud, H. (2008). Analysis of the induced  
344 seismicity of the Lacq gas field (Southwestern France) and model of deformation. *Geophysical Journal*  
345 *International* 172, 1151–1162. doi:10.1111/j.1365-246X.2007.03705.x
- 346 Bishop, I., Styles, P., and Allen, M. (1993). Mining-induced seismicity in the Nottinghamshire Coalfield.  
347 *Quarterly Journal of Engineering Geology and Hydrogeology* 26, 253–279
- 348 Bommer, J. J., Oates, S., Cepeda, J. M., Lindholm, C., Bird, J., Torres, R., et al. (2006). Control of hazard  
349 due to seismicity induced by a hot fractured rock geothermal project. *Engineering Geology* 83, 287 –  
350 306. doi:<https://doi.org/10.1016/j.enggeo.2005.11.002>
- 351 Butcher, A., Luckett, R., Verdon, J. P., Kendall, J.-M., Baptie, B., and Wookey, J. (2017). Local magnitude  
352 discrepancies for near-event receivers: Implications for the UK traffic-light scheme. *Bulletin of the*  
353 *Seismological Society of America* 107, 532–541
- 354 Clarke, H., Eisner, L., Styles, P., and Turner, P. (2014). Felt seismicity associated with shale gas hydraulic  
355 fracturing: The first documented example in Europe. *Geophysical Research Letters* 41, 8308–8314
- 356 Clarke, H., Verdon, J. P., Kettley, T., Baird, A. F., and Kendall, J. (2019). Real-Time Imaging,  
357 Forecasting, and Management of Human-Induced Seismicity at Preston New Road, Lancashire, England.  
358 *Seismological Research Letters* 90, 1902–1915. doi:10.1785/0220190110
- 359 Davies, R., Foulger, G., Bindley, A., and Styles, P. (2013). Induced seismicity and hydraulic fracturing for  
360 the recovery of hydrocarbons. *Marine and Petroleum Geology* 45, 171 – 185. doi:<https://doi.org/10.1016/j.marpetgeo.2013.03.016>

- 362 Deichmann, N. and Giardini, D. (2009). Earthquakes Induced by the Stimulation of an Enhanced  
363 Geothermal System below Basel (Switzerland). *Seismological Research Letters* 80, 784–798. doi:10.  
364 1785/gssrl.80.5.784
- 365 Department of Energy and Climate Change (2013). *Onshore Oil and Gas Exploration in the UK: Regulation  
366 and Best Practice*. Tech. rep.
- 367 Ellsworth, W. L. (2013). Injection-Induced Earthquakes. *Science* 341. doi:10.1126/science.1225942
- 368 Elsworth, D., Spiers, C. J., and Niemeijer, A. R. (2016). Understanding induced seismicity. *Science* 354,  
369 1380–1381. doi:10.1126/science.aal2584
- 370 Foulger, G. R., Wilson, M. P., Gluyas, J. G., Julian, B. R., and Davies, R. J. (2018). Global review of  
371 human-induced earthquakes. *Earth-Science Reviews* 178, 438 – 514
- 372 Fritschen, R. (2010). Mining-Induced Seismicity in the Saarland, Germany. *Pure and Applied Geophysics  
373 - PURE APPL GEOPHYS* 167, 77–89. doi:10.1007/s00024-009-0002-7
- 374 Garcia-Aristizabal, A., Danesi, S., Braun, T., Anselmi, M., Zaccarelli, L., Famiani, D., et al. (2020).  
375 Epistemic Uncertainties in Local Earthquake Locations and Implications for Managing Induced  
376 Seismicity. *Bulletin of the Seismological Society of America* doi:10.1785/0120200100
- 377 Gesret, A., Noble, M., Desassis, N., and Romary, T. (2011). Microseismic monitoring: consequences of  
378 velocity model uncertainties on location uncertainties. In *Third EAGE Passive Seismic Workshop-Actively  
379 Passive 2011*
- 380 Green, P. J. (1995). Reversible jump Markov chain Monte Carlo computation and Bayesian model  
381 determination. *Biometrika* 82, 711–732. doi:10.1093/biomet/82.4.711
- 382 Grigoli, F., Cesca, S., Priolo, E., Rinaldi, A. P., Clinton, J. F., Stabile, T. A., et al. (2017). Current  
383 challenges in monitoring, discrimination, and management of induced seismicity related to underground  
384 industrial activities: A European perspective. *Reviews of Geophysics* 55, 310–340
- 385 Gutenberg, B. (2013). *Seismicity of the earth and associated phenomena* (Read Books Ltd)
- 386 Gutenberg, B. and Richter, C. F. (1942). Earthquake magnitude, intensity, energy, and acceleration. *Bulletin  
387 of the Seismological Society of America* 32, 163–191
- 388 Häring, M. O., Schanz, U., Ladner, F., and Dyer, B. C. (2008). Characterisation of the Basel 1 enhanced  
389 geothermal system. *Geothermics* 37, 469–495
- 390 Hauser, J., Dyer, K. M., Pasmanos, M. E., Bungum, H., Faleide, J. I., Clark, S. A., et al. (2011). A  
391 probabilistic seismic model for the European Arctic. *Journal of Geophysical Research: Solid Earth* 116.  
392 doi:10.1029/2010JB007889
- 393 He, M., Li, Q., and Li, X. (2020). Injection-Induced Seismic Risk Management Using Machine Learning  
394 Methodology – A Perspective Study. *Frontiers in Earth Science* 8, 227. doi:10.3389/feart.2020.00227
- 395 Healy, J. H., Rubey, W. W., Griggs, D. T., and Raleigh, C. B. (1968). The Denver EarthquakeS. *Science*  
396 161, 1301–1310. doi:10.1126/science.161.3848.1301
- 397 Husen, S. and Hardebeck, J. (2010). Earthquake location accuracy. *CORSSA*
- 398 Jaynes, E. T. (2003). *Probability theory: The logic of science* (Cambridge University press)
- 399 Kendall, J.-M., Butcher, A., Stork, A. L., Verdon, J. P., Luckett, R., and Baptie, B. (2019). How big is a  
400 small earthquake? Challenges in determining microseismic magnitudes. *First Break* 37, 51–56
- 401 Keranen, K. M. and Weingarten, M. (2018). Induced Seismicity. *Annual Review of Earth and Planetary  
402 Sciences* 46, 149–174. doi:10.1146/annurev-earth-082517-010054
- 403 Klein, F. W. (2002). *User's guide to HYPOINVERSE-2000, a Fortran program to solve for earthquake  
404 locations and magnitudes*. Tech. rep., US Geological Survey
- 405 Lei, X., Wang, Z., and Su, J. (2019). The December 2018 ML 5.7 and January 2019 ML 5.3 Earthquakes  
406 in South Sichuan Basin Induced by Shale Gas Hydraulic Fracturing. *Seismological Research Letters* 90,

- 407 1099–1110. doi:10.1785/0220190029
- 408 Luckett, R., Ottemöller, L., Butcher, A., and Baptie, B. (2018). Extending local magnitude ML to short  
409 distances. *Geophysical Journal International* 216, 1145–1156
- 410 Majer, E., Nelson, J., Robertson-Tait, A., Savy, J., and Wong, I. (2012). Protocol for addressing induced  
411 seismicity associated with enhanced geothermal systems. *US Department of Energy*, 52
- 412 McGarr, A., Simpson, D., and Seeber, L. (2002). 40 - Case Histories of Induced and Triggered Seismicity.  
413 In *International Handbook of Earthquake and Engineering Seismology, Part A*, eds. W. H. Lee,  
414 H. Kanamori, P. C. Jennings, and C. Kisslinger (Academic Press), vol. 81 of *International Geophysics*.  
415 647 – 661
- 416 Mignan, A., Broccardo, M., Wiemer, S., and Giardini, D. (2017). Induced seismicity closed-form traffic  
417 light system for actuarial decision-making during deep fluid injections. *Scientific Reports* 7, 13607.  
418 doi:10.1038/s41598-017-13585-9
- 419 Myers, S. C., Johannesson, G., and Hanley, W. (2007). A Bayesian hierarchical method for multiple-event  
420 seismic location. *Geophysical Journal International* 171, 1049–1063
- 421 Ottemöller, L. and Sargeant, S. (2013). A local magnitude scale ML for the United Kingdom. *Bulletin of  
422 the Seismological Society of America* 103, 2884–2893
- 423 Poliannikov, O. V., Prange, M., Malcolm, A., and Djikpesse, H. (2013). A unified Bayesian framework for  
424 relative microseismic location. *Geophysical Journal International* 194, 557–571
- 425 Rawlinson, N. and Sambridge, M. (2004). Multiple reflection and transmission phases in complex layered  
426 media using a multistage fast marching method. *GEOPHYSICS* 69, 1338–1350. doi:10.1190/1.1801950
- 427 Schultz, R., Beroza, G., Ellsworth, W., and Baker, J. (2020). Risk-Informed Recommendations for  
428 Managing Hydraulic Fracturing–Induced Seismicity via Traffic Light Protocols. *Bulletin of the  
429 Seismological Society of America* 110. doi:10.1785/0120200016
- 430 Van Thienen-Visser, K. and Breunese, J. (2015). Induced seismicity of the Groningen gas field: History  
431 and recent developments. *The Leading Edge* 34, 664–671
- 432 Zhang, X., Curtis, A., Galetti, E., and de Ridder, S. (2018). 3D Monte Carlo Surface Wave Tomography.  
433 *Geophysical Journal International* 215, 1644–1658. doi:10.1093/gji/ggy362
- 434 Zhang, X., Roy, C., Curtis, A., Nowacki, A., and Baptie, B. (2020). Imaging the subsurface using induced  
435 seismicity and ambient noise: 3D Tomographic Monte Carlo joint inversion of earthquake body wave  
436 travel times and surface wave dispersion. *Geophysical Journal International* doi:10.1093/gji/ggaa230

Figure 1.JPG

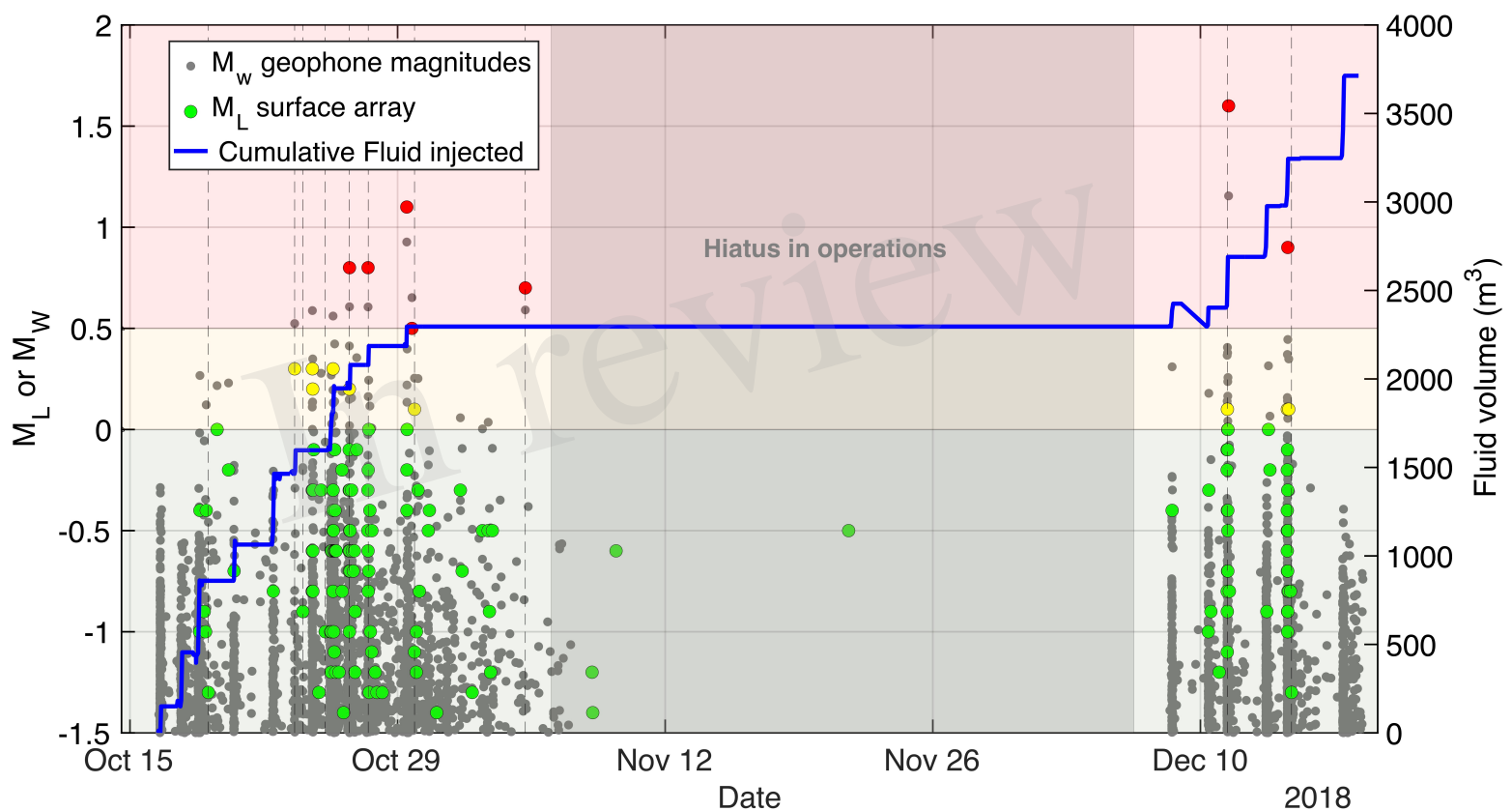


Figure 2.JPG

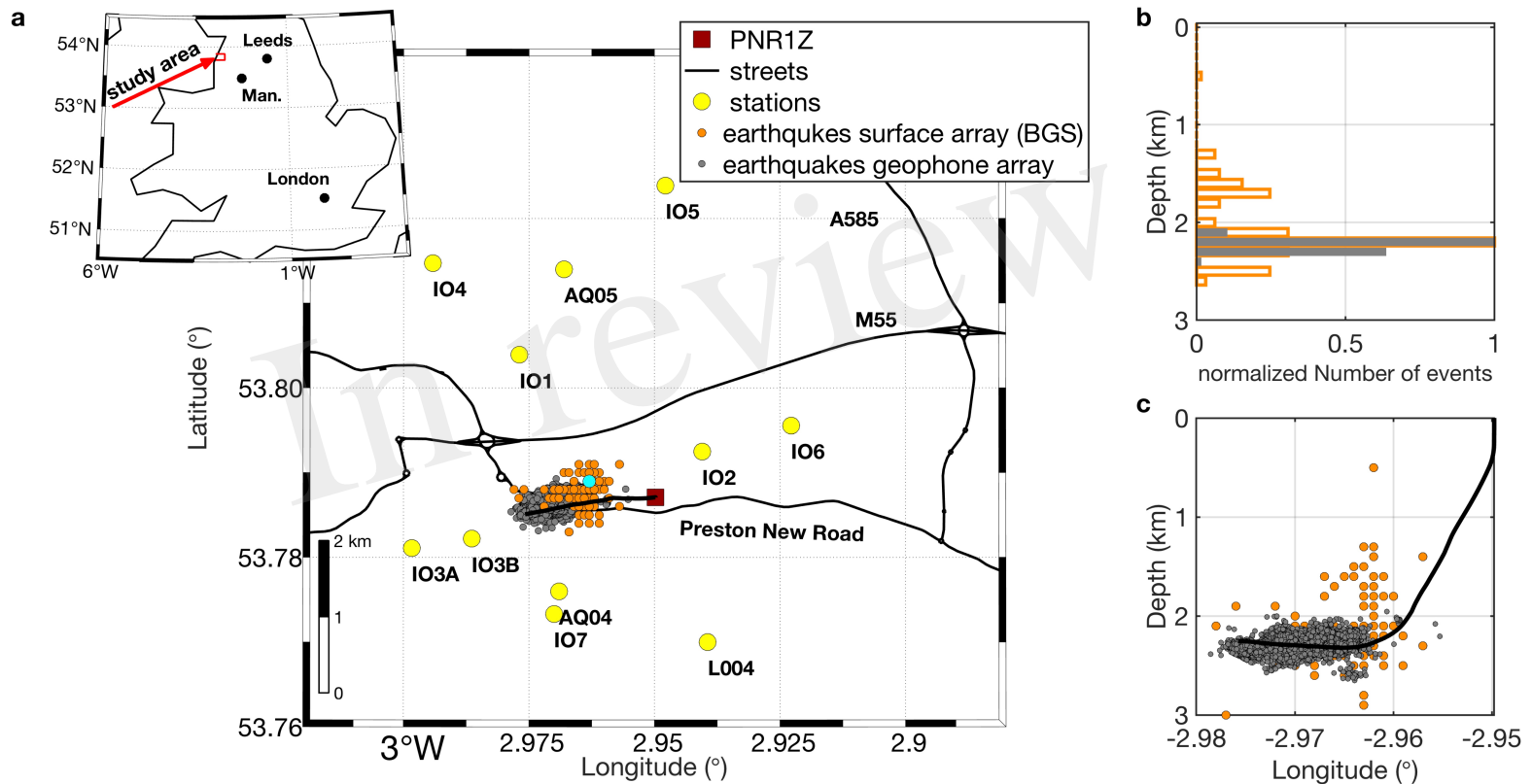


Figure 3.JPG

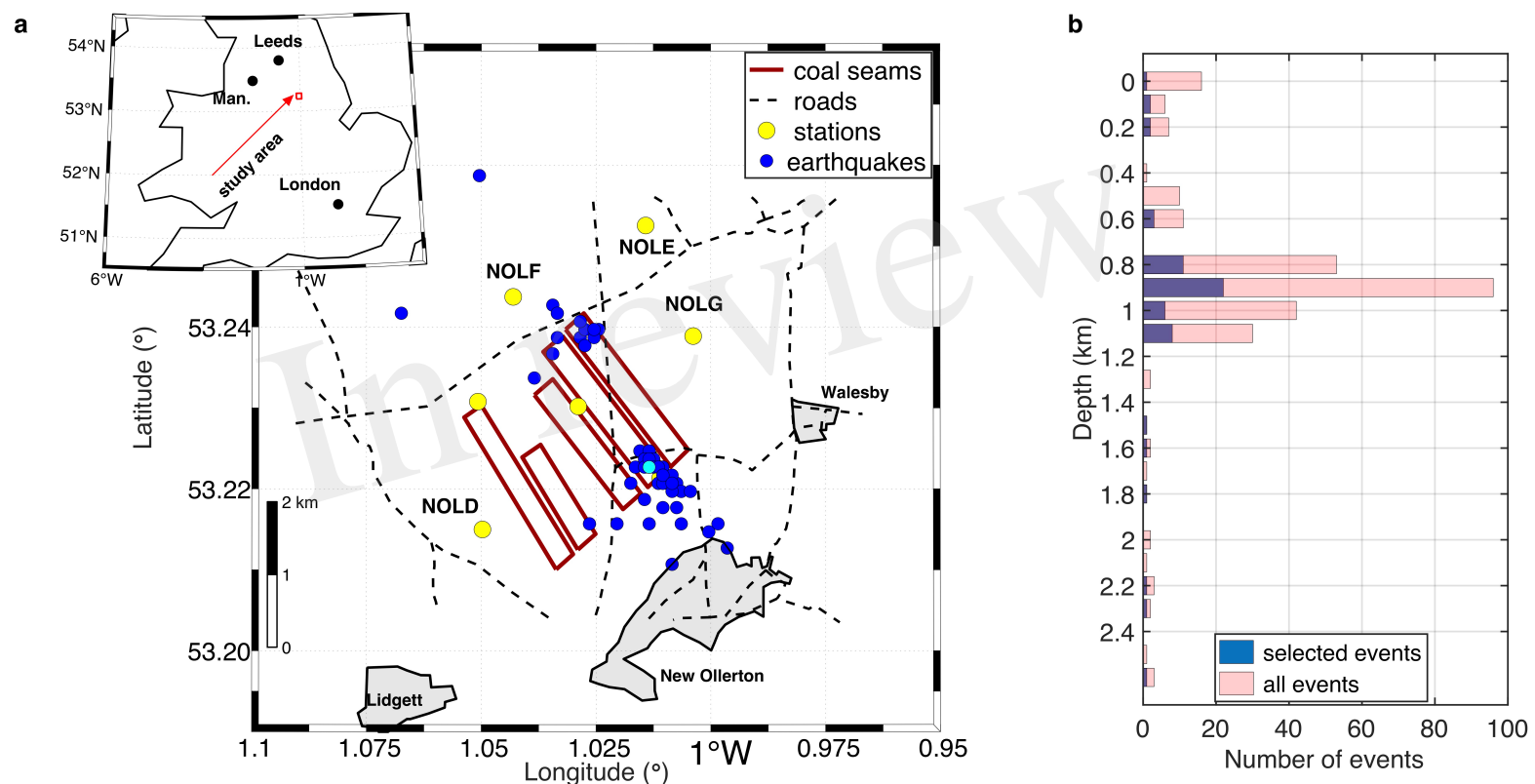


Figure 4.JPG

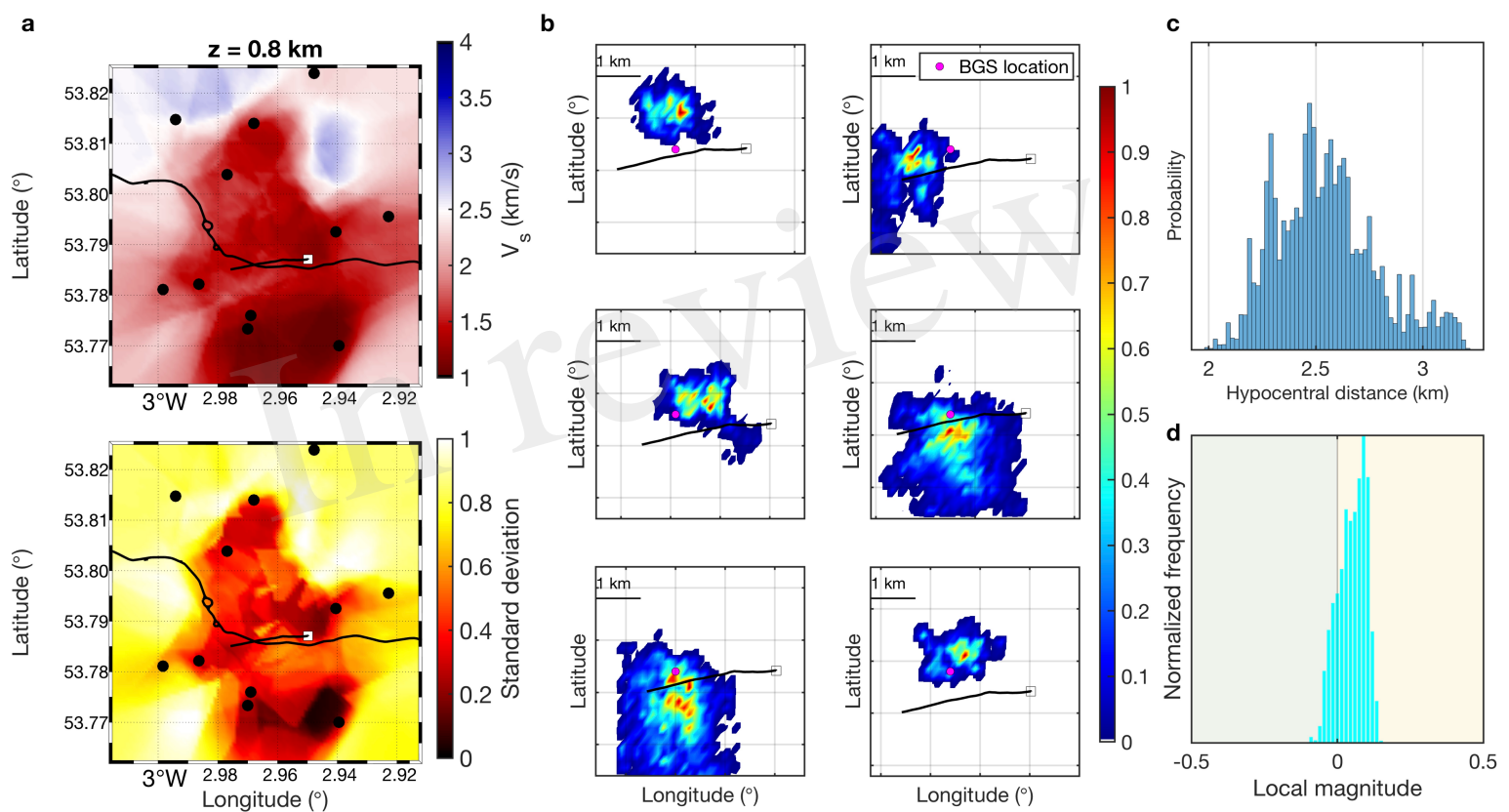


Figure 5.JPEG

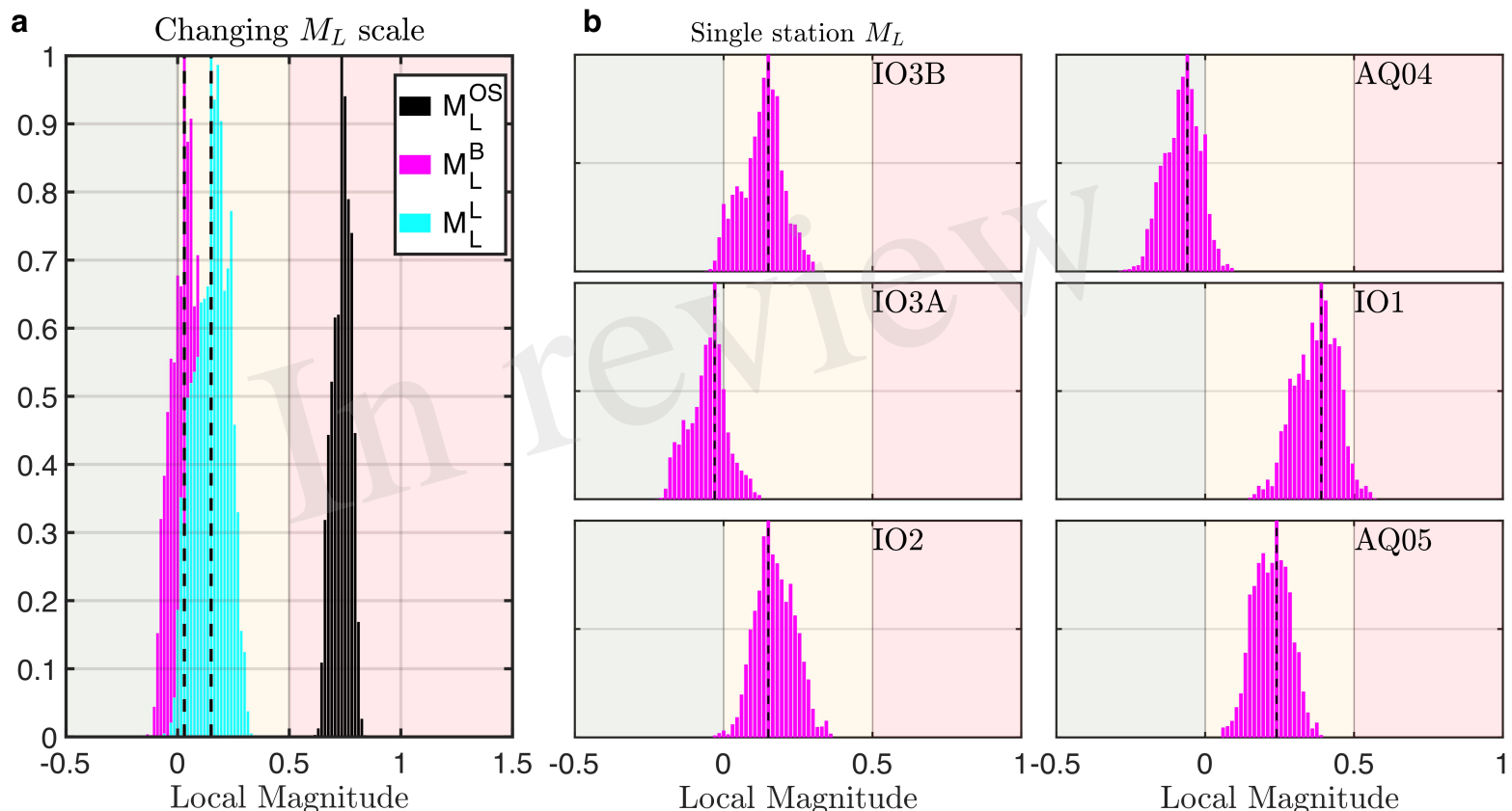


Figure 6.JPG

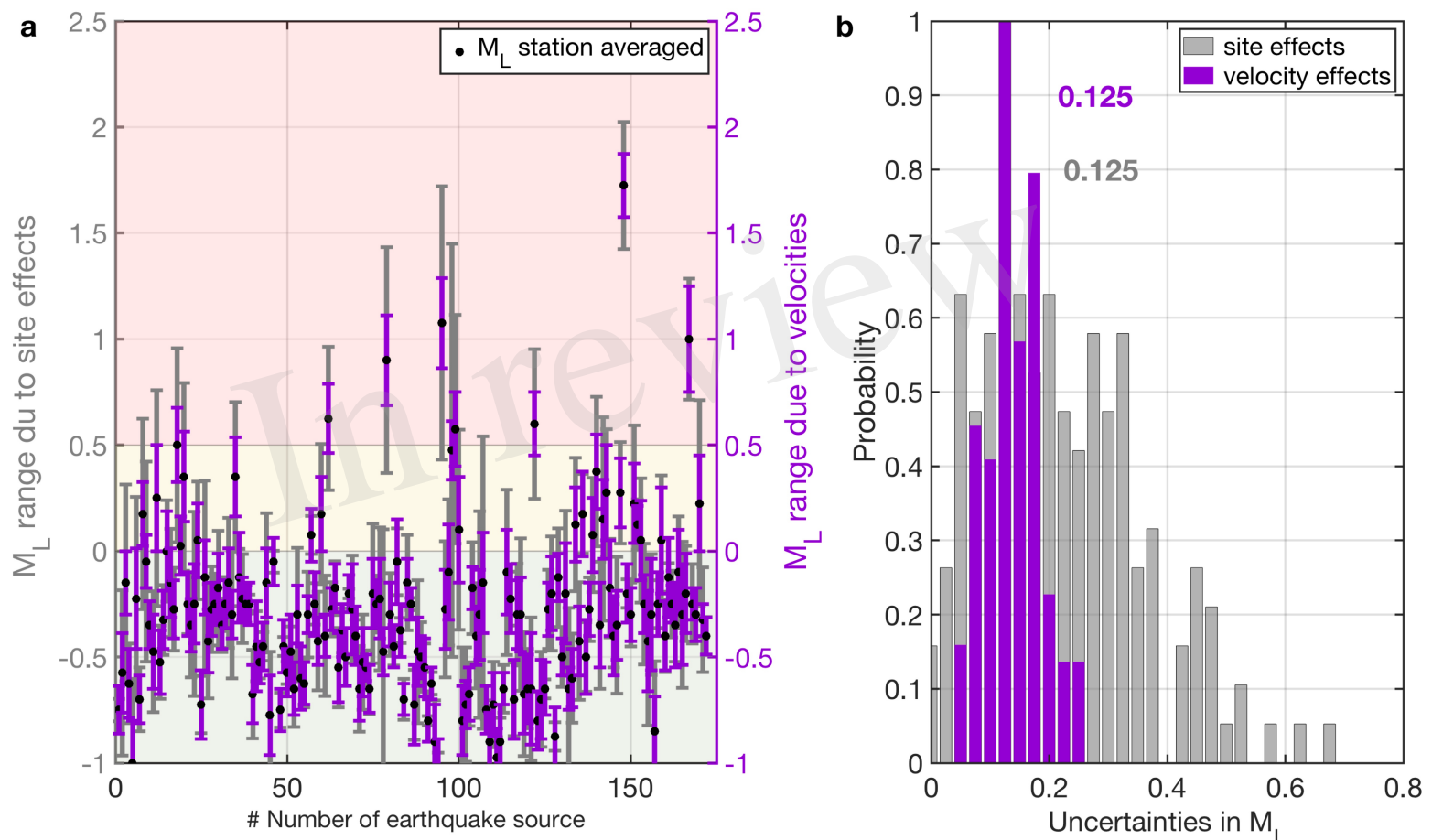


Figure 7.JPEG

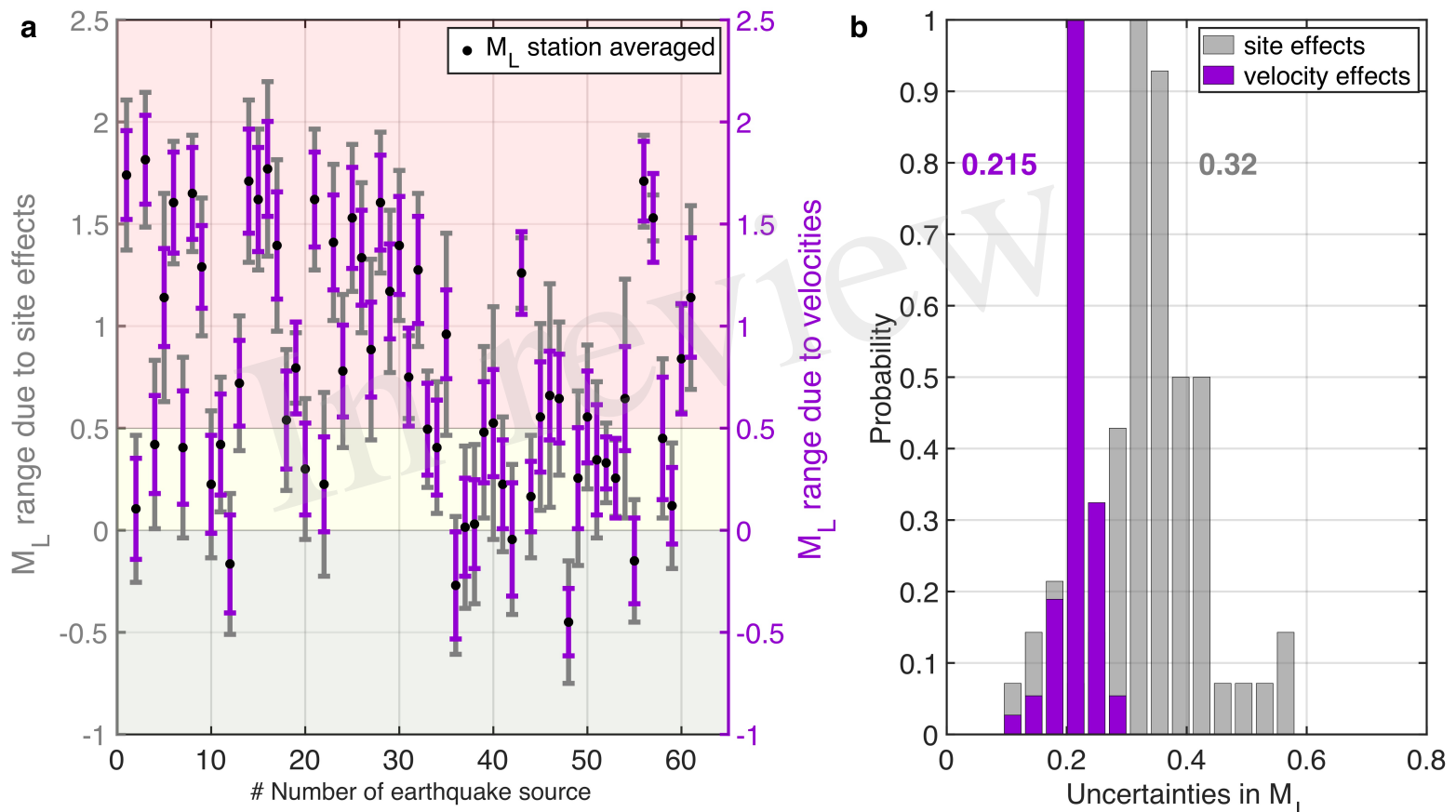


Figure 8.JPG

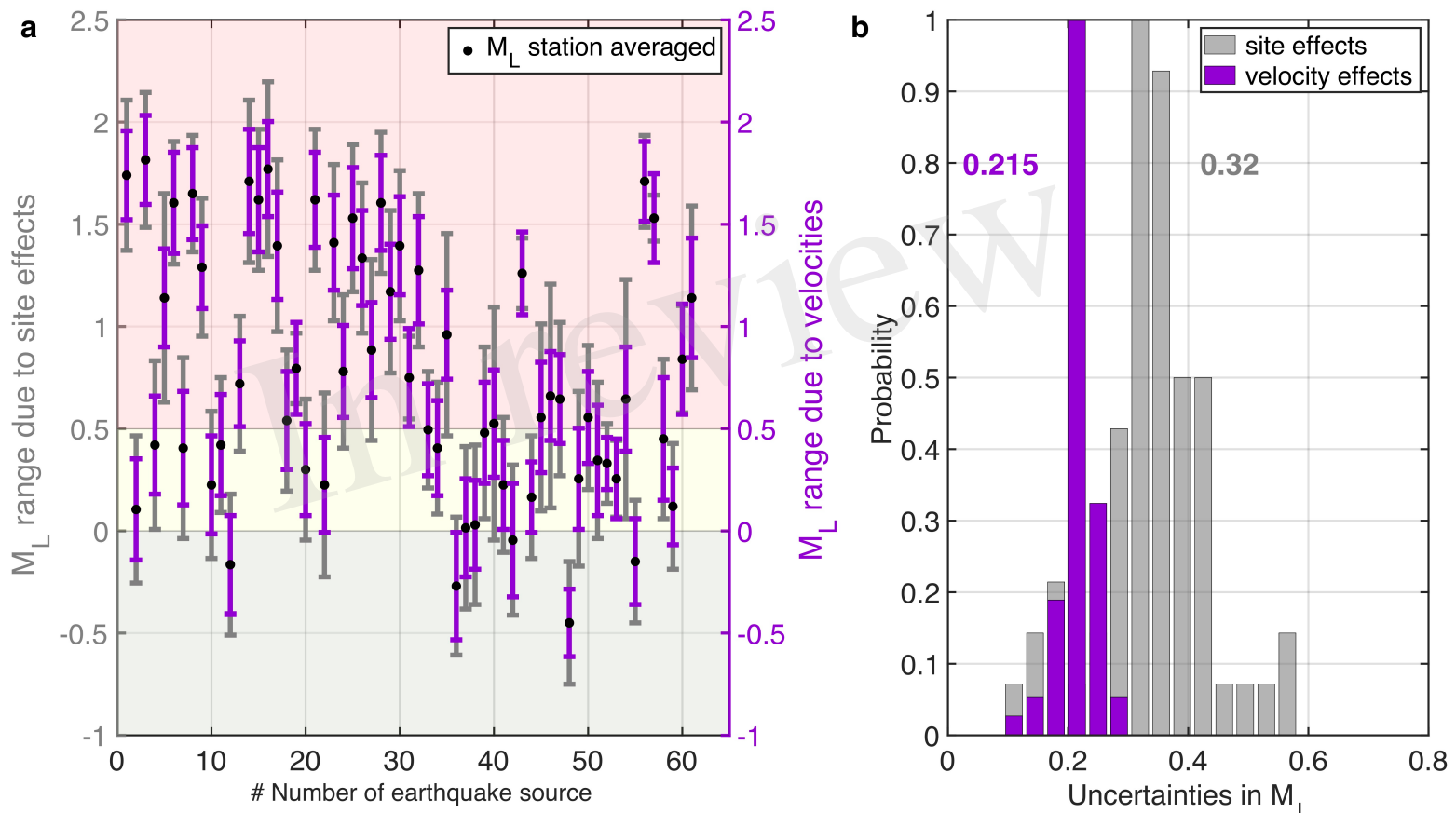


Figure 9.JPG

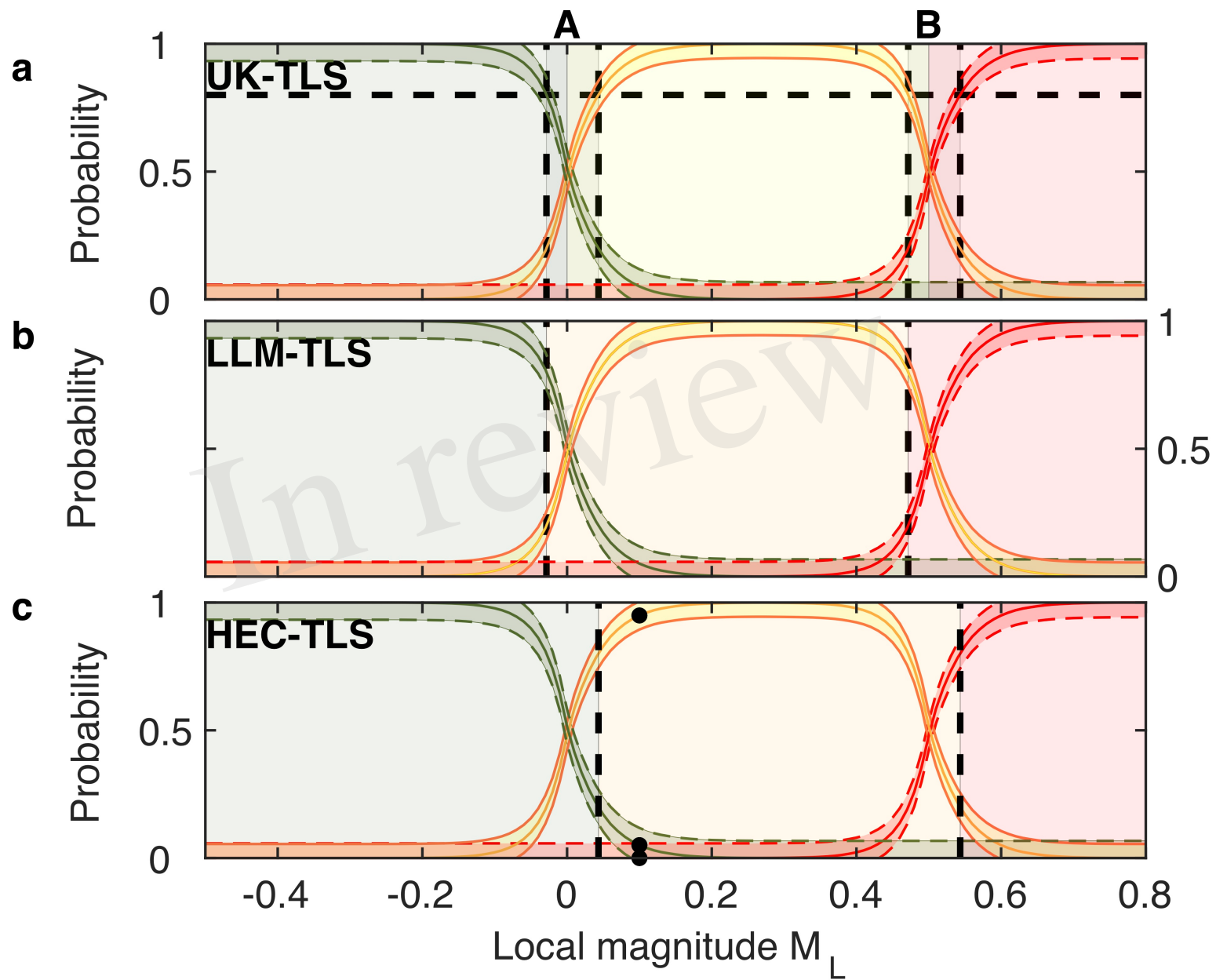


Figure 10.JPEG

